



| | |
|----------------------------------|--|
| Publication Year | 2019 |
| Acceptance in OA | 2020-12-30T09:06:43Z |
| Title | The origin of R CrA variability. A complex triple system hosting a disk |
| Authors | Sissa, E., GRATTON, Raffaele, ALCALA', JUAN MANUEL, DESIDERA, Silvano, MESSINA, Sergio, MESA, DINO, D'ORAZI, VALENTINA, RIGLIACO, ELISABETTA |
| Publisher's version (DOI) | 10.1051/0004-6361/201936101 |
| Handle | http://hdl.handle.net/20.500.12386/29327 |
| Journal | ASTRONOMY & ASTROPHYSICS |
| Volume | 630 |

SN 2016B a.k.a. ASASSN-16ab: a transitional Type II supernova

Raya Dastidar^{1,2*}, Kuntal Misra^{1,3}, Mridweeka Singh^{1,4}, D. K. Sahu⁵,
A. Pastorello⁶, Anjasha Gangopadhyay^{1,4}, L. Tomasella⁶, S. Benetti⁶, G. Terreran⁷,
Pankaj Sanwal^{1,4}, Brijesh Kumar¹, Avinash Singh^{5,8}, Brajesh Kumar⁵,
G. C. Anupama⁵ and S. B. Pandey¹

¹Aryabhata Research Institute of Observational Sciences, Manora Peak, Nainital 263 001, India

²Department of Physics & Astrophysics, University of Delhi, Delhi 110 007, India

³Department of Physics, University of California, 1 Shields Ave, Davis, CA 95616-5270, USA

⁴Pt. Ravi Shankar Shukla University, Raipur 492 010, India

⁵Indian Institute of Astrophysics, Koramangala, Bengaluru 560 034, India

⁶INAF Osservatorio Astronomico di Padova, Vicolo dell'Osservatorio 5, I-35122 Padova, Italy

⁷Center for Interdisciplinary Exploration and Research in Astrophysics (CIERA) and Department of Physics and Astronomy, Northwestern University, Evanston, IL 60208, USA

⁸Joint Astronomy Programme, Department of Physics, Indian Institute of Science, Bengaluru 560 012, India

Accepted 2019 April 1. Received 2019 January 8; in original form 2018 October 29

ABSTRACT

We present photometry, polarimetry, and spectroscopy of the Type II supernova ASASSN-16ab/SN 2016B in PGC 037392. The photometric and spectroscopic follow-up commenced about 2 weeks after shock breakout and continued until nearly 6 months. The light curve of SN 2016B exhibits intermediate properties between those of Type IIP and IIL. The early decline is steep (1.68 ± 0.10 mag 100 d⁻¹), followed by a shallower plateau phase (0.47 ± 0.24 mag 100 d⁻¹). The optically thick phase lasts for 118 d, similar to Type IIP. The ⁵⁶Ni mass estimated from the radioactive tail of the bolometric light curve is 0.082 ± 0.019 M_⊙. High-velocity component contributing to the absorption trough of H α and H β in the photospheric spectra are identified from the spectral modelling from about 57–97 d after the outburst, suggesting a possible SN ejecta and circumstellar material interaction. Such high-velocity features are common in the spectra of Type IIL supernovae. By modelling the true bolometric light curve of SN 2016B, we estimated a total ejected mass of ~ 15 M_⊙, kinetic energy of ~ 1.4 foe, and an initial radius of ~ 400 R_⊙.

Key words: techniques: photometric – techniques: polarimetric – techniques: spectroscopic – supernovae: general – supernovae: individual: ASASSN-16ab/SN 2016B – galaxies: individual: PGC 037392.

1 INTRODUCTION

The classification of supernovae (SNe), from the 1940s to present, has been through numerous challenges. With the detailed study of events, their individual properties surfaced, which led to the proposal of various classes of SNe. Type II SNe are the result of the core-collapse of massive stars ($\gtrsim 8$ M_⊙), showing abundant hydrogen in their spectra at peak. In order of increasing hydrogen envelope stripping, Type II SNe are classified into II-plateau (IIP), II-linear (IIL), and IIb. The hydrogen-rich Type II SNe viz. IIP and IIL, are categorized based on the presence of a roughly constant luminosity phase or a linearly declining photospheric

phase, respectively, in their optical light curve, at epochs post peak brightness (Barbon, Ciatti & Rosino 1979).

There has been a long-standing debate over classifying SNe II into Type IIP and IIL, which has recently escalated by sample studies of Type II SNe, some advocating while others disfavoured the classification. The studies of Arcavi et al. (2012) and Faran et al. (2014) prescribe to retain the historic classification, whereas Anderson et al. (2014) and Sanders et al. (2015) believe that the distinction stem from the paucity in observed Type IIL SNe as well as the limited time for which these events are generally observed, due to the rapid decline in their brightness compared to SNe IIP. This led Anderson et al. (2014) to propose a more reasonable nomenclature viz. classifying hydrogen-rich explosions simply as SNe II with a mention of its plateau decline rate parameter. Observationally, strong P-Cygni profiles of H I lines in the spectra

* E-mail: rdastidr@gmail.com

are the typical signatures of Type II SNe, while their light curves exhibit a range of morphologies. These differences possibly arise due to the varying mass and density profile of the hydrogen envelope of the progenitor star at the time of explosion or may be an effect of dense circumstellar material surrounding the progenitor (Morozova, Piro & Valenti 2017).

While many theoretical studies are trying to provide a plausible explanation of the explosion mechanism of these events, observationally, the explosion geometry of SNe is a key diagnostic to constrain their explosion mechanism. However, owing to the unresolvability of extragalactic sources, the precise determination of ejecta structure and geometry becomes arduous. Nevertheless, the recent simulations of exploding stars, which require a multidimensional explosion scenario for a successful outburst (e.g. Melson, Janka & Marek 2015; Müller 2016; Roberts et al. 2016), is a definitive cue of the asymmetric nature of these explosions. The polarization of the emitted radiation from SNe may be attributed to this (Höfllich et al. 1996; Höfllich, Wheeler & Wang 1999; Wang et al. 2003b; Leonard et al. 2006), others being electron scattering in the SN ejecta (Jeffery 1991; Dessart & Hillier 2011) and the reflection of light from the circumstellar and the interstellar material (Chevalier 1986; Wang et al. 1996; Mauerhan et al. 2017). Broad-band polarimetry and spectropolarimetry prove to be handy to decode the imprints of polarization engraved in the emitted radiation (see Wang & Wheeler 2008, for a review). While the overall structure of the ejecta can be understood from the spectra of SNe, polarimetric studies reveal the shape, composition, opacity, and ionization state of the SN ejecta.

Type IIP SNe are expected to show low levels of continuum polarization at early times (~ 0.1 per cent) and an increasing trend in polarization levels (~ 1 per cent) as the inner layers of the ejecta are revealed (Leonard & Filippenko 2001; Leonard et al. 2002b; Chornock et al. 2010; Kumar et al. 2016; Mauerhan et al. 2017), which might stem from an aspherical core (Chugai et al. 2005; Chugai 2006). However, Dessart & Hillier (2011) and Leonard et al. (2016) attributed the rise in polarization levels to the decreasing electron scattering opacity at late times. So the initial low polarization might be electron scattering optical depth effect, rather than arising from a spherical envelope. The early-time asphericity, thus, gets subdued by the photons scattered off multiple times by the electrons, which in the process loses all its memory of the initial polarization state.

In this paper, we present the results of the monitoring campaign of a Type II event, ASASSN-16ab/SN 2016B, in the galaxy PGC 037392. The paper is organized as follows: Section 2 presents the parameters of SN 2016B and in Section 3 we discuss the data acquired and the reduction procedure. The estimation of total line of sight extinction is discussed in Section 4. The photometric evolution and light-curve parameter estimates are discussed in Section 5. The polarization measurements and the derived parameters are described in Section 6. The bolometric light curve, ^{56}Ni mass, and explosion parameters from analytical modelling of the bolometric light curve are derived in Section 7. We present the spectral evolution, SYN++ modelling and derive line velocities and an estimate of the progenitor mass of SN 2016B in Section 8. In Section 9, we discuss the transitional nature of SN 2016B and summarize the results in Section 10.

2 SN 2016B

SN 2016B, a.k.a. ASASSN-16ab, was spotted in PGC 037392 by the All Sky Automated Survey for SuperNovae (ASAS-SN) programme

Table 1. Basic information on SN 2016B and the host galaxy PGC 037392. The host galaxy parameters are taken from NED.

| | |
|-----------------------------|-------------------------------------|
| Host galaxy | PGC 037392 |
| Galaxy type | Scd |
| Redshift | 0.004293 ± 0.000077^a |
| Major diameter | 0.59 arcmin |
| Minor diameter | 0.39 arcmin |
| Helio. radial velocity | $1287 \pm 23 \text{ km s}^{-1}$ |
| Offset from nucleus | 9'8 W, 4'6 S |
| Distance | $26.8 \pm 4.9 \text{ Mpc}^b$ |
| Total extinction $E(B - V)$ | $0.075 \pm 0.017 \text{ mag}^c$ |
| SN type | II |
| Date of discovery | 2457 389.12 (JD) |
| Estimated date of explosion | $2457 382.0 \pm 1.2 \text{ (JD)}^c$ |

^aBeers et al. (1995).

^bTully–Fisher method.

^cThis paper.

Table 2. The best three matches to the spectrum obtained on 2016 January 7 along with the rlap parameter to estimate the age of SN 2016B.

| SN | rlap ^a | Age since V_{max} (d) | Age since explosion (d) |
|-----------|-------------------|--------------------------------|-------------------------|
| SN 2004et | 10.2 | −1.9 | 14.2 ± 3 |
| SN 2004et | 8.8 | −0.9 | 15.2 ± 3 |
| SN 1999em | 8.6 | −2.9 | 11.3 ± 5 |
| Mean | | | 14.2 ± 2.0 |

^aQuality of fit.

on 2016 January 3.62 UT at a visual magnitude of 14.7 mag (Shappee et al. 2016). The SN was located at approximately 4'6 S and 9'8 W from the centre of the host galaxy. Considering the Tully–Fisher distance to the galaxy, which is $26.8 \pm 4.9 \text{ Mpc}$ (Karachentsev, Nasonova & Karachentseva 2015, reported in NED), the deprojected radial distance of the SN from the host galaxy nucleus is 2.3 kpc. The SN was also detected by ASAS-SN in images obtained on 2015 December 27.5 UT at $V \sim 16.3 \text{ mag}$ and the last non-detection to a magnitude limit of $V > 16.7 \text{ mag}$ was reported on 2015 December 24.5 UT. The intermediate epoch between the last non-detection and first detection tightly constrain the explosion epoch to 2015 December 26 UT (JD $2457 382.5 \pm 1.5$). A classification spectrum was obtained on 2016 January 04.11 UT using the SPRAT spectrograph on the Liverpool Telescope located at Roque de los Muchachos (Piascik & Steele 2016), which is consistent with a pre-maximum Type II SN spectrum. The details of SN 2016B and its host galaxy are given in Table 1.

We used the SNID code (Blondin & Tonry 2007) to cross-correlate the spectrum obtained by us on 2016 January 7 UT to the library of spectral templates in SNID and constrain the explosion epoch. We perform the fit in the wavelength range 3500–6000 Å since during early phase most of the spectral lines in SNe II lie in this range. We report the best three matches in Table 2 along with the quality of fit ‘rlap’ parameter and obtain a mean value of $14.2 \pm 2.0 \text{ d}$ as the epoch of the spectrum from the explosion date. This yields 2015 December 24.7 UT (JD $2457 381.2 \pm 2.0$) as the explosion epoch of SN 2016B. This is in good agreement to that obtained from non-detection. The consistency of the two methods has also been indicated in the works of Anderson et al. (2014) and Gutiérrez et al. (2017). The mean of these two values yields 2015 December 25.4 UT (JD $2457 382.0 \pm 1.2$), which we have adopted as the explosion date of SN 2016B.

3 DATA ACQUISITION AND REDUCTION

3.1 Photometry and spectroscopy

Optical monitoring of SN 2016B was conducted using the telescopes listed in Table A1, equipped with broad-band *UBVRI* and *ugriz* filters from ~ 13 to 188 d post explosion. A single epoch of observation was obtained on 465 d since the estimated explosion time in the *R* band with the 3.6m Devasthal Optical Telescope (DOT). The *ugriz* magnitudes were converted to *UBVRI* magnitudes using the transformation equations in Jordi, Grebel & Ammon (2006). The SN was also observed from ~ 9 to 23 d post explosion with the Ultra-Violet/Optical Telescope (UVOT; Roming et al. 2005) in three UV (*uvw2*: $\lambda_c = 1928 \text{ \AA}$, *uvm2*: $\lambda_c = 2246 \text{ \AA}$, *uvw1*: $\lambda_c = 2600 \text{ \AA}$) and three optical (*u*, *b*, *v*) filters on The Neil Gehrels *Swift* Observatory (Gehrels et al. 2004). The UV data reduction is discussed in Appendix A and the magnitudes are provided in Table A2. The optical images were reduced after the initial cleaning steps as discussed in Appendix A and the differential magnitudes of the SN (presented in Table A4) were obtained using the nightly zero-points computed from the local standards generated in the SN field (see Fig. A1 and Table A3). The spectroscopic observations were carried out at 18 epochs from the facilities listed in Table A1 and the log of spectroscopic observation is tabulated in Table B1. The spectroscopic reduction procedure is detailed in Appendix B.

3.2 Polarimetry

The broad-band polarimetric observations of SN 2016B in the *R* band ($\lambda_{\text{eff}} = 6700 \text{ \AA}$) were made using the ARIES Imaging Polarimeter (AIMPOL; Rautela, Joshi & Pandey 2004) mounted at the 1.04m Sampurnanand Telescope (ST) at Manora Peak, Nainital. The observations were carried out at seven epochs during 2016 January to March using the liquid nitrogen cooled Tektronix $1024 \times 1024 \text{ pixel}^2$ CCD camera. However, only the central $370 \times 370 \text{ pixel}^2$ CCD region was used for the observation. The pixel scale of the CCD in this set-up is $1.48 \text{ arcsec pixel}^{-1}$ which corresponds to an unvignetted field of view covering ~ 8 arcmin diameter of sky. The stellar full width at half-maximum (FWHM) is found to be well-constrained within 2–3 pixels.

A half-wave plate modulator and a Wollaston prism analyser are used inside AIMPOL, which produce the ordinary and extraordinary images separated by 28 pixels along the north–south direction on the sky plane. Multiple frames are acquired at each of the four half-wave plate positions (i.e. 0° , 22.5° , 45° , and 67.5°), which are then aligned and combined to increase the signal-to-noise ratio. The ratio of the difference between the intensities of the ordinary (I_o) and extraordinary (I_e) beams to the total intensity is given by

$$R(\alpha) = \frac{I_e/I_o - 1}{I_e/I_o + 1} = P \cos(2\theta - 4\alpha), \quad (1)$$

where P is the fraction of the total light in the linearly polarized condition, θ is the position angle of the plane of polarization, and α is the half-wave plate position angle. This ratio is denoted by normalized Stokes' parameters $q(=Q/I)$, $u(=U/I)$, $q_1(=Q_1/I)$, and $u_1(=U_1/I)$ when the half-wave plate's fast axis is rotated by $\alpha = 0^\circ$, 22.5° , 45° , and 67.5° , respectively with respect to the reference axis. Ideally, P and θ can be determined from the measurements of the first two plate positions. However, due to varying response of the system to the two orthogonal components and the dependence of the response of CCD on the position of its surface, a correction factor is multiplied with the ratio of the observed signal in the two

images (I_e/I_o) given by the following expression (Ramaprakash et al. 1998):

$$\frac{F_o}{F_e} = \left[\frac{I'_o(0^\circ)}{I'_e(45^\circ)} \times \frac{I'_o(45^\circ)}{I'_e(0^\circ)} \times \frac{I'_o(22.5^\circ)}{I'_e(67.5^\circ)} \times \frac{I'_o(67.5^\circ)}{I'_e(22.5^\circ)} \right]^{0.25}. \quad (2)$$

Applying this correction factor, we derive the ratio at the four plate positions and fitting the cosine curve, the values of P and θ are obtained. The errors in the measured ratios are limited by photon statistics and is given by (Ramaprakash et al. 1998),

$$\sigma_{R(\alpha)} = \frac{\sqrt{N_e + N_o + N_{Be} + N_{Bo}}}{(N_e + N_o)}, \quad (3)$$

where N_o and N_e are ordinary and extraordinary counts and N_{Bo} and N_{Be} are ordinary and extraordinary background counts, respectively, for a position α . This error is then propagated to derive the errors in the polarization parameters.

We observed two polarized standards (HD 19820 and HD 25443, from Schmidt, Elston & Lupie 1992) for calibration of the zero-point polarization angle, which mainly arises from the imperfect alignment of the fast axis of half-wave plate with the north–south direction. The measured degree of polarization (P) of the polarized standards are listed in Table 3 and were found to be consistent within error with the standard values and any deviation from the standard values of the polarization angle (θ) is applied to the SN. The instrumental polarization of ST has been characterized since 2004 by observations of various sources (Medhi et al. 2008; Pandey et al. 2009; Eswaraiyah et al. 2013; Kumar et al. 2014; Srivastav et al. 2016) and is found to be ~ 0.1 per cent in *UBVRI* bands. We applied this correction in our SN polarization measurements.

4 EXTINCTION

The intrinsic nature of an event is unveiled once the reddening contributions from the Milky Way and the host galaxy along its line of sight are discerned. The Schlafly & Finkbeiner (2011) IR based dust map estimates a colour excess $E(B - V)$ of 0.0180 ± 0.0012 mag for Galactic extinction in the direction of SN 2016B.

To estimate host galaxy extinction, use of empirical relations correlating the equivalent width of Na I D narrow absorption line to the colour excess has been done for a number of SNe, even though it has been shown to be a poor indicator (Phillips et al. 2013). The rest-frame low-resolution spectra of SN 2016B, however, does not exhibit any conspicuous narrow absorption feature around 5893 \AA , possibly indicating low levels of host galaxy extinction. This agrees with the remote location of the SN in its host galaxy, free of any nearby contaminating sources.

Consequently, we resorted to the ‘colour method’ (Olivares et al. 2010) to estimate the host galaxy extinction in SN 2016B. In this method, the opacity of SNe IIP is assumed to be dominated by electron scattering. Since all SNe IIP will attain nearly the same recombination temperature at the end of the plateau phase, these ought to have similar intrinsic colours at this phase (Hamuy & Pinto 2002). Hence, the different colours exhibited by SNe IIP at these epochs may be attributed to reddening due to dust along its line of sight. The conversion factor computed by Olivares et al. (2010) between $E(V - I)$ and A_V using a library of SN II spectra is 2.518 and the following prescription is suggested:

$$A_V(V - I) = 2.518[(V - I) - 0.656] \quad (4)$$

$$\sigma(A_V) = 2.518 \sqrt{\sigma_{(V-I)} + 0.0053^2 + 0.0059^2}. \quad (5)$$

Table 3. Polarization measurements in the R band for standard stars.

| Star ID | Standard ^a | | UT date (yyyy-mm-dd) | Observed | |
|----------|-----------------------|----------------|-------------------------|------------------|-----------------|
| | P_R (per cent) | θ_R (°) | | P_R (per cent) | θ_R (°) |
| HD 19820 | 4.53 ± 0.03 | 114.46 ± 0.16 | 2016-01-10.9 | 4.176 ± 0.166 | 123.167 ± 1.141 |
| | | | 2016-01-15.0 | 4.414 ± 0.226 | 124.184 ± 1.465 |
| | | | 2016-01-16.0 | 4.590 ± 0.138 | 126.442 ± 0.860 |
| | | | 2016-02-08.0 | 4.396 ± 0.113 | 126.863 ± 0.736 |
| HD 25443 | 4.73 ± 0.32 | 133.65 ± 0.28 | 2016-01-10.9 | 4.408 ± 0.116 | 142.629 ± 0.756 |
| | | | 2016-01-13.0 | 4.658 ± 0.142 | 143.230 ± 0.875 |
| | | | 2016-01-15.0 | 5.003 ± 0.117 | 143.012 ± 0.673 |
| | | | 2016-01-16.0 | 4.582 ± 0.133 | 143.265 ± 0.828 |
| | | | 2016-02-09.0 | 4.696 ± 0.143 | 138.343 ± 0.872 |
| | | | 2016-03-08.0 | 4.720 ± 0.074 | 143.255 ± 0.452 |

^aTaken from Schmidt et al. (1992)

We calculate the weighted mean of $(V - I)$ colours (corrected for Galactic extinction) on 97.3 and 104.4 d from the explosion corresponding to the end of the plateau phase, which results in $(V - I) = 0.726 \pm 0.021$ mag. The estimated $A_{V(host)}$ is 0.176 ± 0.054 mag and with a total-to-selective extinction ratio (R_V) of 3.1, we obtain $E(B - V)_{host} = 0.057 \pm 0.017$ mag. Hence, the total reddening to the SN, considering the contributions from both the Milky Way and host galaxy reddening is $E(B - V)_{tot} = 0.075 \pm 0.017$ mag, which we have adopted throughout the paper.

5 PHOTOMETRIC EVOLUTION OF SN 2016B

The light-curve slope and luminosities of the early declining part, plateau phase, and radioactive tail phase provide clues to our understanding of the nature and energetics of the explosion. The decline rates during these phases indicate the extent of thermalization in the ejecta, with shallow slopes of the plateau and the radioactive tail suggesting massive ejecta retained by the progenitor star (Young 2004). To examine the behaviour of SN 2016B, we concocted a comparison sample of SNe with a variety of early decline rates in V band; SNe 2004et (Sahu et al. 2006; Misra et al. 2007; Maguire et al. 2010), 2007od (Inserra et al. 2011), 2009bw (Inserra et al. 2012), 2009dd (Inserra et al. 2013), 2013ej (Bose et al. 2015; Huang et al. 2015; Dhungana et al. 2016; Yuan et al. 2016), and 2016esw (de Jaeger et al. 2018) have decline rates between 0.5 and 1.0 mag in the first 50 d after maximum; SN 2013by (Valenti et al. 2015), a typical SN IIL, exhibits the highest decline rate (1.5 mag in 50 d) while SN 1999em (Hamuy et al. 2001; Leonard et al. 2002a, 2003) displays the lowest decline rate (0.25 mag in 50 d). We also include the peculiar Type II SN 1987A (Hamuy & Suntzeff 1990) in the comparison sample.

The UV and optical light curves of SN 2016B are presented in Fig. 1. The observed multiband light curves of SN 2016B commences with a decline, which characterizes the initial expansion and cooling of the ejecta. The UV light curve steeply declines in the first 25 d at a rate of 0.20 ± 0.01 mag d^{-1} in $uvw1$ and 0.23 ± 0.01 mag d^{-1} in both $uvw2$ and $uvm2$ bands. The $UBVRI$ light curve then enters the plateau phase supported by the heating from the recombination of the initially shock ionized hydrogen. At the end of the plateau phase, the SN luminosity starts to decay in the tail phase which is powered by the instantaneous energy deposition from the decay of ^{56}Co to ^{56}Fe .

In order to determine the light-curve parameters, we fit the V -band light curve with the equation given in Olivares et al. (2010):

$$y(t) = \frac{-a_0}{1 + e^{(t-t_{PT})/w_0}} + p_0 \times (t - t_{PT}) + m_0 - P e^{-\left(\frac{t-Q}{R}\right)^2}, \quad (6)$$

where t is the time since explosion in days, t_{PT} is the time in days from explosion to the transition point between the end of the plateau and start of the radioactive tail phase, a_0 is the depth of the drop from plateau to nebular phase, w_0 assesses the width of the transition phase in days, p_0 constrains the slope of radioactive tail, P is the height of the Gaussian peak in units of magnitude, Q is the centre of the Gaussian function in days, and R is the width of the Gaussian function. From the best fit (as shown in Fig. 2), we obtain $t_{PT} = (133.5 \pm 2.6)$ d and the magnitude drop from plateau to tail phase (a_0) to be 1.6 ± 0.2 mag in a span of 25 d.

We apply the distance and reddening corrections to derive the V -band absolute magnitudes of SN 2016B and other SNe II (see Fig. 3). The distance and extinction values for the comparison sample are listed in Table 4. The absolute V -band light curve of SN 2016B shows a gradual decline up to about 66 d ($\sim 0.84 \pm 0.05$ mag $50 d^{-1}$), thereafter it settles on to a roughly constant magnitude phase lasting up to 118 d since explosion (0.24 ± 0.12 mag $50 d^{-1}$). These values are estimated by fitting a smoothed piecewise linear function to the apparent V -band magnitudes:

$$m_v = a + a_1 t + a_2 \left(\frac{t - T_{tran}}{2} + \sqrt{\frac{(t - T_{tran})^2}{4} + b} \right). \quad (7)$$

The break time (T_{tran}) is the transition time from the early declining phase to the plateau phase, a_1 is the slope of the early declining phase, $(a_1 + a_2)$ is the slope of the plateau phase, and b is the smoothing factor. The two slopes (s_1 and s_2) from the best fit are shown in Fig. 2 and could possibly be arising from a density discontinuity in the ejecta of SN 2016B. The optically thick phase duration (OPTd), defined in Anderson et al. (2014) as the time span from explosion until the extrapolated plateau is more luminous than the light curve by 0.1 mag, is ~ 118 d (marked with a vertical dashed line in Fig. 2). We fit both equations (6) and (7) on the V -band light curve of the comparison sample and list the parameters for the sample in Table 5.

The effective plateau duration of SN 2016B is very short, however, we note that the OPTd is longer than any other SNe IIL and is similar to SNe IIP (usually lasting for more than 80 d in SNe IIP). The evolution is similar to SN 2009bw, whose early decline rate (0.95 mag $50 d^{-1}$) is higher than SN 2016B by ~ 0.1 mag, but has a similar plateau length and plateau slope. SN 2016esw shows similar duration of the early declining phase lasting nearly 60 d, however, the slopes are steeper than SN 2016B. The light curve of SN 2016B becomes flatter thereafter, with a slope similar to the archetypal Type IIP SN 1999em (0.25 mag $50 d^{-1}$), unlike SN 2013ej which continues to decline at a steady rate until it transitions to the radioactive tail.

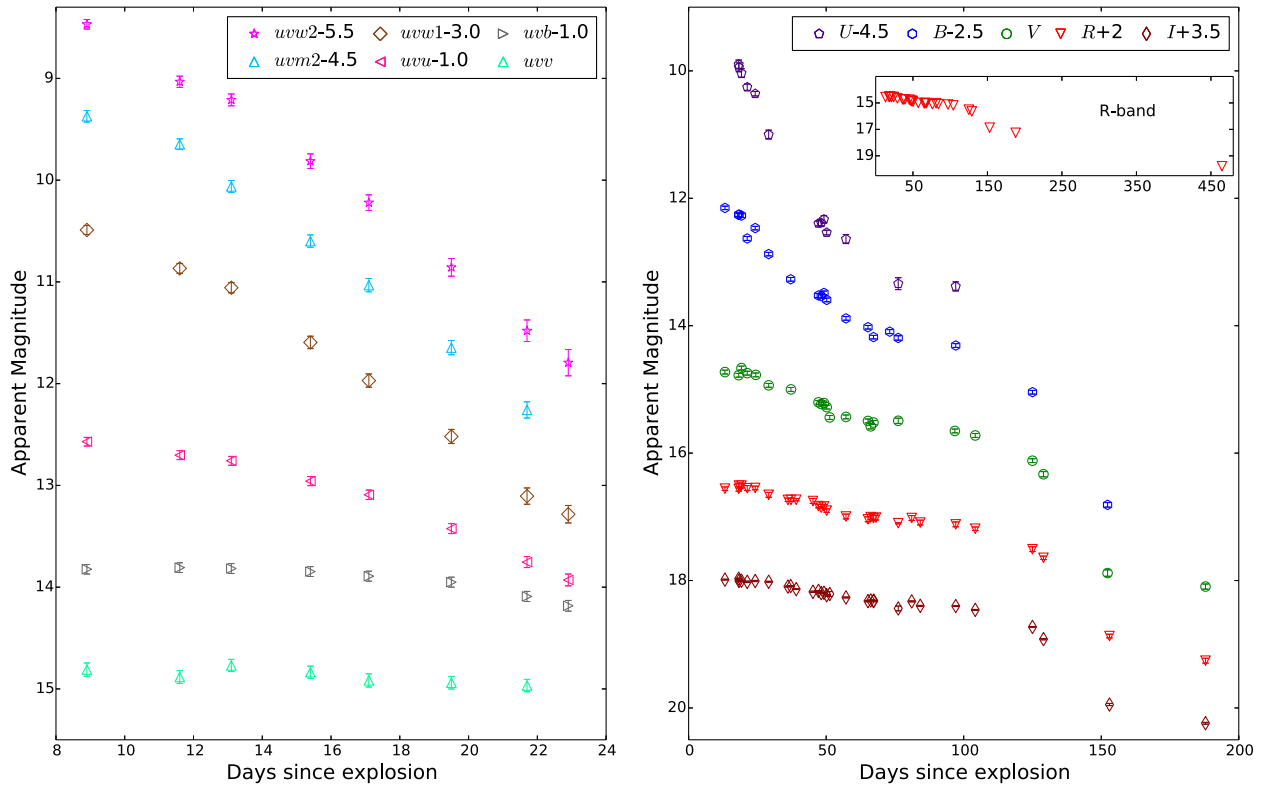


Figure 1. *Swift* UVOT (left-hand panel) and broad-band *UBVR I* (right-hand panel) light curves of SN 2016B shifted arbitrarily for clarity. The inset plot in the right-hand panel shows the *R*-band light curve up to the last point obtained on 465 d with the 3.6m DOT.

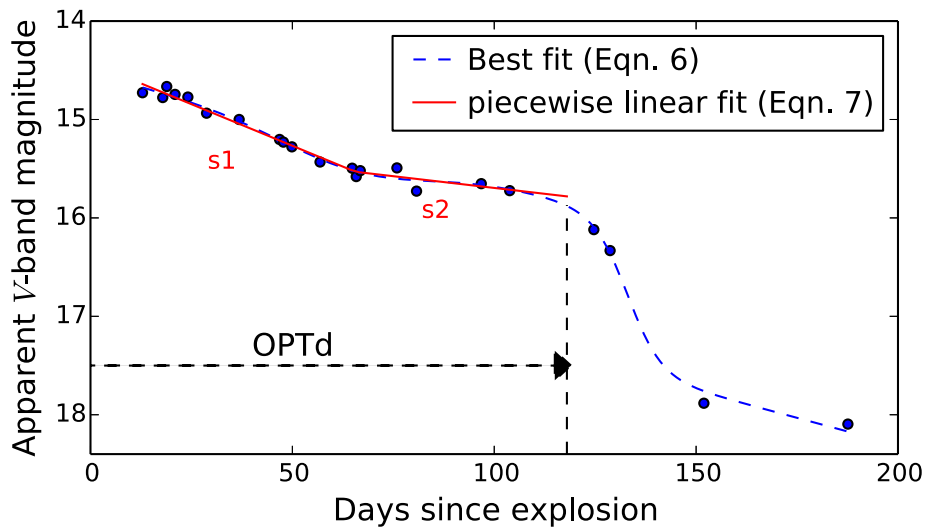


Figure 2. The *V*-band light curve of SN 2016B fitted with the expression given in Olivares et al. (2010) shown with the (blue) dashed lines. The red lines are from the fit with the piecewise linear function to the light curve with an early declining phase (s_1) and a plateau phase (s_2). The dashed vertical line denotes the end of the plateau phase.

While the light-curve parameters, viz. the slope of the early cooling phase ($s_1 = 1.68 \pm 0.10 \text{ mag } 100 \text{ d}^{-1}$) and the plateau slope ($s_2 = 0.47 \pm 0.24 \text{ mag } 100 \text{ d}^{-1}$) of SN 2016B, are consistent with those of SNe II derived by Anderson et al. (2014) ($s_1 = 2.65 \pm 1.50$ and $s_2 = 1.27 \pm 0.93 \text{ mag } 100 \text{ d}^{-1}$) within the errors, SN 2016B has a higher OPTd value. Further, we note that the decline

rate of SN 2016B in *V* and *R* bands in the first 50 d (0.84 and 0.52 mag, respectively), requires SN 2016B to be classified as SN IIL (Li et al. 2011; Faran et al. 2014). Moreover, the early decline rates in *B* band, which is $3.88 \text{ mag } 100 \text{ d}^{-1}$ ($>3.5 \text{ mag } 100 \text{ d}^{-1}$ for SNe IIL, Patat et al. 1994), place SN 2016B in the IIL subclass. Despite the overall similarity of the *V*-band light curve to

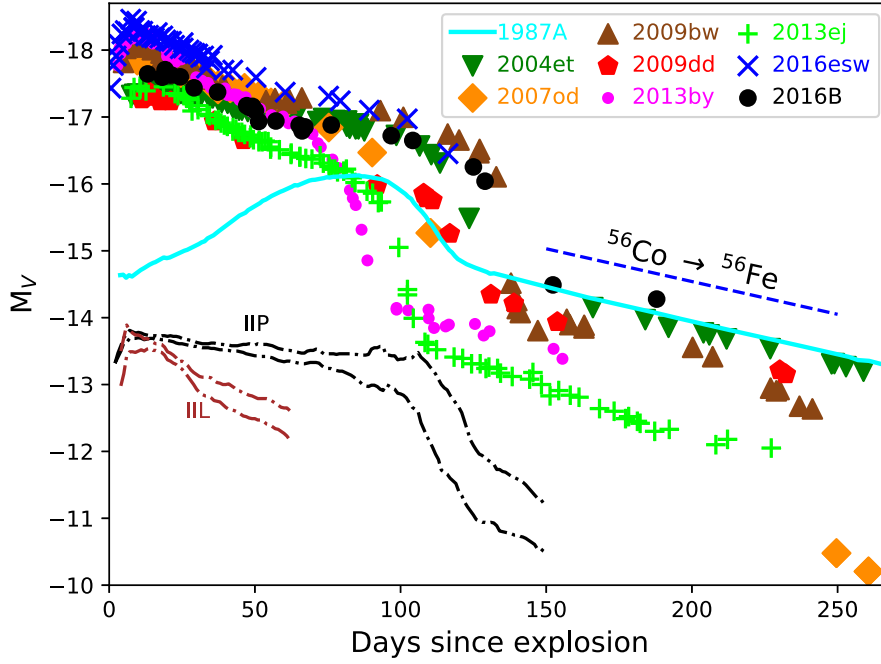


Figure 3. Comparison of absolute V -band light curves of SN 2016B with other Type II SNe. The magnitudes are corrected for distance and reddening as listed in Table 4. The radioactive decay line assuming full trapping of photons is shown with dashed lines. The dash-dotted lines depict the range of slopes of Type IIP and IIL SNe as presented in Faran et al. (2014).

Table 4. Parameters of the SNe II sample.

| Supernova | Parent Galaxy | Distance ^a (Mpc) | A_V^{tot} (mag) | M_V (mag) | OPTd (d) | E (10^{51} erg) | R (R_\odot) | M_{ej} (M_\odot) | ^{56}Ni (M_\odot) | Ref. |
|--------------|-------------------|-----------------------------|-------------------|---------------|--------------|----------------------|---------------------|------------------------|-------------------------------------|-------------------|
| 1987A | LMC | 0.05 | 0.60 | – | 40 | 1.3 | 40 | 15 | 0.075 | 1 |
| 1999em | NGC 1637 | 11.7 (0.1) | 0.31 | –16.71 | 95 | $1.2^{+0.6}_{-0.3}$ | 249^{+243}_{-150} | 27^{+14}_{-8} | $0.042^{+0.027}_{-0.019}$ | 2,3,4 |
| 2004et | NGC 6946 | 5.4 (1.0) | 1.27 | –17.04 | 110 ± 10 | 0.98 ± 0.25 | 530 ± 280 | 16 ± 5 | 0.06 ± 0.03 | 5,6,7 |
| 2007od | UGC 12846 | 25.3 (0.8) | 0.12 | –17.64 | 25 | 0.5 | 670 | 5–7 | 0.02 | 8 |
| 2009bw | UGC 2890 | 20.2 (0.6) | 0.96 | –17.24 | 100 | 0.3 | 510–1000 | 8.3–12 | 0.022 | 9 |
| 2009dd | NGC 4088 | 14.0 (0.4) | 1.40 | –16.6 | ~100 | 0.2 | 719 | 8.0 | 0.029 | 10 |
| 2013by | ESO 138-G10 | 14.74 (1.0) | 0.60 | –17.12 (0.11) | 75 | – | – | – | 0.029 | 11 |
| 2013ej | NGC 628 | 9.6 (0.7) | 0.19 | –16.61 (0.10) | 85 | 2.3 | 450 | 12 | 0.020 | 12 |
| 2016esw | UGC 2890 | 118.1 | 0.74 | –17.24 | 105 | 1.0 | 190 | – | – | 13 |
| 2016B | PGC 037392 | 26.8 (4.9) | 0.23 | –16.80 | 118 | 1.4 | 400 | 14.7 | 0.082 ± 0.019 | This paper |

References: (1) Hamuy & Suntzeff (1990), (2) Hamuy et al. (2001), (3) Leonard et al. (2002a), (4) Leonard et al. (2003), (5) Sahu et al. (2006), (6) Misra et al. (2007), (7) Maguire et al. (2010), (8) Inserra et al. (2011), (9) Inserra et al. (2012), (10) Inserra et al. (2013), (11) Valenti et al. (2015), (12) Huang et al. (2015); Bose et al. (2015); Yuan et al. (2016); Dhungana et al. (2016), (13) de Jaeger et al. (2018).

^aIn the $H_0 = 73.24 \text{ km s}^{-1} \text{ Mpc}^{-1}$ scale (Riess et al. 2016).

Table 5. Best-fitting values of t_{PT} , a_0 using (Olivares et al. 2010) expression and s_1 , s_2 using smoothed piecewise linear function.

| SN | t_0 JD (2400 000+) | $t_0 - t_{PT}$ (d) | a_0 (mag) | s_1 | s_2 | T_{tran} | References |
|------------|-------------------------|-----------------------|-----------------|-----------------|-----------------|------------|------------|
| SN 1999em | 51 477.0 (1.0) | 112.6 ± 1.4 | 2.20 ± 0.17 | 0.50 ± 0.06 | – | – | 1,2 |
| SN 2004et | 53 270.5 (0.2) | 123.9 ± 3.4 | 2.11 ± 0.06 | 1.27 ± 0.14 | 0.74 ± 0.15 | 43 ± 5 | 3,4,5 |
| SN 2009bw | 54 916.5 (3.0) | 135.3 ± 2.5 | 2.31 ± 0.23 | 1.90 ± 0.07 | 0.43 ± 0.17 | 49 ± 5 | 6 |
| SN 2013by | 56 404.0 (2.0) | 86.5 ± 0.4 | 2.56 ± 0.23 | 3.47 ± 0.20 | 2.35 ± 0.24 | 28 ± 2 | 7 |
| SN 2013ej | 56 497.5 (0.3) | 99.7 ± 0.3 | 2.82 ± 0.04 | 3.21 ± 0.28 | 1.63 ± 0.33 | 41 ± 2 | 8,9,10 |
| SN 2016esw | 57 608.3 (0.2) | – | – | 1.83 ± 0.06 | 1.02 ± 0.27 | 60 ± 9 | 11 |
| SN 2016B | 57 382.0 (1.2) | 133.5 ± 2.6 | 1.6 ± 0.2 | 1.68 ± 0.10 | 0.47 ± 0.24 | 66 ± 5 | This paper |

References: (1) Hamuy et al. (2001), (2) Leonard et al. (2002a), (3) Sahu et al. (2006) (4) Misra et al. (2007), (5) Maguire et al. (2010), (6) Inserra et al. (2012), (7) Valenti et al. (2015), (8) Bose et al. (2015), (9) Dhungana et al. (2016), (10) Yuan et al. (2016), (11) de Jaeger et al. (2018).

the SN II family, the correlation found by Anderson et al. (2014) between the absolute peak magnitude and the slope of the plateau ($M_V = -1.12 \times s_2 - 15.99$ mag) is not followed by SN 2016B. For the observed maximum absolute magnitude $M_V = -17.7$ mag (which may not be peak magnitude), the correlation predicts plateau slope greater than $1.5 \text{ mag } 100 \text{ d}^{-1}$. This is significantly higher than the observed slope of $0.47 \text{ mag } 100 \text{ d}^{-1}$. SN 2016esw was also found to deviate from the correlation, leading de Jaeger et al. (2018) to suggest important implications for cosmology with SNe II.

The temporal evolution of the reddening-corrected broad-band colours serves as an important piece of information to understand the dynamics of SN ejecta. The reddening-corrected colour evolution $[(B - V)_0, (V - R)_0, \text{ and } (V - I)_0]$ of SN 2016B is shown in Fig. 4, with those of other SNe from the comparison sample. The $(B - V)_0$ colour becomes redder by 0.6 mag in 50 d, with indicates the cooling of the ejecta. In fact, this trend is seen in the $(V - R)_0$ and $(V - I)_0$ colours, which become redder at a much slower rate. This is because of the slowly evolving magnitude in the *VRI* bands at early phase. While the $(B - V)_0$ colour of SNe 2013by and 2013ej shows a bluer trend in the nebular phase, we do not find any perceptible trend in SN 2016B, similar to SNe 2009bw and 2009dd. Nevertheless, the overall evolution of SN 2016B is similar to most of comparison SNe II.

6 BROAD-BAND POLARIMETRY

Polarimetric observations of SN 2016B in the *R* band have been carried out at seven epochs during 16.4–73.5 d from explosion. The intrinsic polarization of the SN is contaminated by polarization of the SN light induced by aspherical dust grains along the SN line of sight. This additive component, the interstellar polarization (ISP), should be eliminated from the observed SN polarization value before claiming any polarization intrinsic to the SN. The ISP is formed by two components along the line of sight: polarization induced by the dust grains in the Milky Way (MW) and the host galaxy. However, there is no well-established method to determine these components as most of these methods rely on certain assumptions which are not always fulfilled. Below we discuss the methods used to estimate the MW and the host galaxy polarization.

6.1 Estimation of Milky Way polarization

For SN 2016B, we determine the ISP using the field stars, observed in the same frame as SN 2016B. We selected three bright field stars and list their polarization parameters and distance (taken from *Gaia* DR2; Gaia Collaboration 2016, 2018) in Table 6. The ISP is computed from the observed stars by averaging over the Stokes parameters as follows:

$$\begin{aligned} \langle Q \rangle &= \langle P_i \cos(2\theta_i) \rangle_{i=1..n} \\ \langle U \rangle &= \langle P_i \sin(2\theta_i) \rangle_{i=1..n}, \end{aligned} \quad (8)$$

which are then converted back to polarization parameters using:

$$\begin{aligned} P_{MW} &= \sqrt{\langle Q \rangle^2 + \langle U \rangle^2}; \\ \theta_{MW} &= \frac{1}{2} \tan^{-1} \left(\frac{\langle U \rangle}{\langle Q \rangle} \right). \end{aligned} \quad (9)$$

The mean ISP_{MW} parameters, we obtain, are $P_{MW} = 0.43 \pm 0.04$ per cent and $\theta_{MW} = (83 \pm 4)^\circ$ for SN 2016B.

6.2 Estimation of host galaxy polarization

Estimating the host galaxy polarization is a non-trivial task. While now we know the Galactic dust properties, the characteristics of dust in the host galaxy remain largely unknown. These studies are possible in nearby galaxies, with two known cases of SNe 1986G (Hough et al. 1987) and 2001el (Wang et al. 2003a), where it was inferred that the dust grain sizes are smaller than Galactic ones. Assuming that the dust grain properties of PGC 037392 is similar to Galactic dust, we roughly estimate the maximum degree of polarization due to host galaxy following Serkowski, Mathewson & Ford (1975) relation, $P_{max} < 9 \times E(B - V)$. For extinction values of host galaxy estimated in Section 3, we obtain P_{max} (for host) to be < 0.68 per cent for SN 2016B. Next, we require the magnetic field direction information for the host, to perform the subtraction of this component from the total component. It is well-established that the magnetic field runs parallel to the spiral arms in spiral galaxies. However, even being an Scd-type galaxy, the spiral arms of PGC 037392 are not well-resolved, neither the position of the SN, given the large inclination of the galaxy. So, we restrain from subtracting host galaxy component from the total polarization.

6.3 Estimation and evolution of intrinsic polarization

The intrinsic polarization of the SN is computed by vectorially subtracting the ISP_{MW} from the observed SN polarization. The evolution of degree of polarization and the polarization angle during the photospheric phase of SN 2016B are presented in top and middle panel of Fig. 5 along with the *R*-band light-curve evolution in this period in the bottom panel. The polarization parameters are tabulated in Table 7. Since we have not subtracted the host galaxy polarization from the observed values, we caution the reader that these values are over- or underestimates of the intrinsic polarization (depending on the polarization angle of the host galaxy). While the ISP subtracted polarization remains nearly constant to 1 per cent during the observation period from the early declining phase to the plateau phase, there is an abrupt change in the polarization angle at 73.5 d by $\sim 100^\circ$. The polarization angle in SN 2004dj has also been observed to change by 30° during the fall from the plateau to the radioactive tail phase. In SN 2004dj, the possible reasons conjectured were the gradual unveiling of ^{56}Ni in the inner regions distributed along the equatorial plane as the SN enters the nebular phase or likely an effect of opacity (Leonard et al. 2006). Nevertheless, in the absence of a good estimate of the ISP, suggesting a change in polarization angle is inconsequential due to its strong dependence on the degree of alignment of the ISP with the dominant axis of the SN ejecta. In the presence of a significant ISP, changes in the amount of polarization at fixed angle may be manifested as a change in polarization angle, arising the possibility of a change in the intrinsic polarization percentage in the final epoch and not just the angle. However, since we do not have another nearby epoch of polarimetric observation of SN 2016B, we defer from making any firm conclusion.

In Fig. 6, we compare the polarization parameters of SN 2016B with SNe 1987A (Barrett 1988), 1999em (Leonard et al. 2001), 2004dj (Leonard et al. 2006), 2005af (Pereyra et al. 2006), 2012aw (Kumar et al. 2014), 2013ej (Mauerhan et al. 2017), and 2013hj (Bose et al. 2016). The polarization parameters of SN 1999em are obtained from *V*-band polarimetry, although, the evolution in *R* band is expected to be similar. SNe 2013ej and 2016B exhibit the maximum polarization (> 1 per cent) in the sample. The rest of the SNe except SN 2013hj show polarization values below

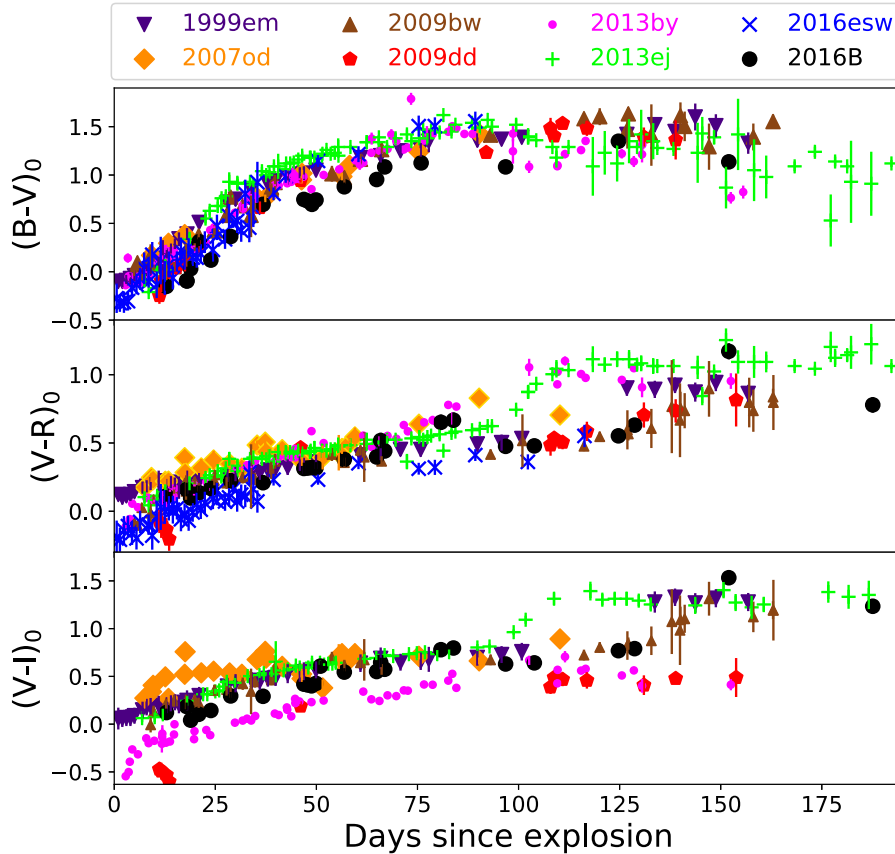


Figure 4. The $(B - V)_0$, $(V - R)_0$, and $(V - I)_0$ colour evolution of SN 2016B compared with other SNe II.

Table 6. Polarization measurements in the R band of the field stars as marked in Fig. A1 towards the direction of SN 2016B.

| #id | $\alpha_{J2000.0}$ (hh:mm:ss) | $\delta_{J2000.0}$ (dd:mm:ss) | P_R (per cent) | θ_R ($^\circ$) | Distance (pc) |
|-----|----------------------------------|----------------------------------|---------------------|----------------------------|------------------|
| E | 11:55:16.7 | +01:44:18.5 | 0.28 ± 0.08 | 75.4 ± 7.9 | 679 |
| G | 11:55:15.0 | +01:41:44.8 | 0.33 ± 0.14 | 80.8 ± 8.8 | 900 |
| I | 11:55:11.1 | +01:44:02.6 | 0.25 ± 0.06 | 90.5 ± 4.9 | 193 |

0.5 per cent. However, considering the maximum host galaxy polarization, coaligned with the SN polarization, the intrinsic polarization of SN 2016B will drop down to ~ 0.4 per cent, similar to most SNe II.

7 EXPLOSION PARAMETERS

7.1 Bolometric light curve

We compute the pseudo-bolometric luminosities of SN 2016B using $BVRI$ magnitudes following the method described in Dastidar et al. (2018), which include SED integration using the trapezoidal rule over the photometric fluxes after correcting for extinction and distance. The zero-points to convert the dereddened $BVRI$ magnitudes to fluxes are taken from Bessell, Castelli & Plez (1998). Note that the B -band magnitude on 188.1 d is computed from the $(B - V)$ colour which becomes nearly constant at the late phases. We compared the pseudo-bolometric light curves of SN 2016B with those of other SNe from the comparison sample in Fig. 7,

constructed using the same method to maintain consistency. The shape of light curve of SN 2016B resembles that of SN 2007od. The evolution after the initial decline is similar to SNe 2004et and 2009bw, except that SN 2016B has a shorter effective plateau length and a more luminous radioactive tail compared to these two events, the latter indicating a greater amount of ^{56}Ni synthesized. The tail phase luminosity is rather similar to SN 1987A.

Further, to estimate the explosion parameters such as the ^{56}Ni mass, the explosion energy, and the ejecta mass, modelling of the true bolometric light curve is necessary. The true bolometric luminosities can be obtained by taking into account the contributions from the ultraviolet (UV) to the infrared (IR) bands. We construct the true bolometric light curve using the direct integration module in SuperBoL (Lusk & Baron 2017) that is based on the method given in Bersten & Hamuy (2009). This involves extrapolating the SED to the UV and IR regimes, assuming the SED to be blackbody. At later times, when the ejecta becomes optically thin and the SN can no longer be approximated by a blackbody, a linear extrapolation is performed in the UV wavelengths. We use the pseudo-bolometric luminosity to estimate the ^{56}Ni mass in Section 7.2.1 and the

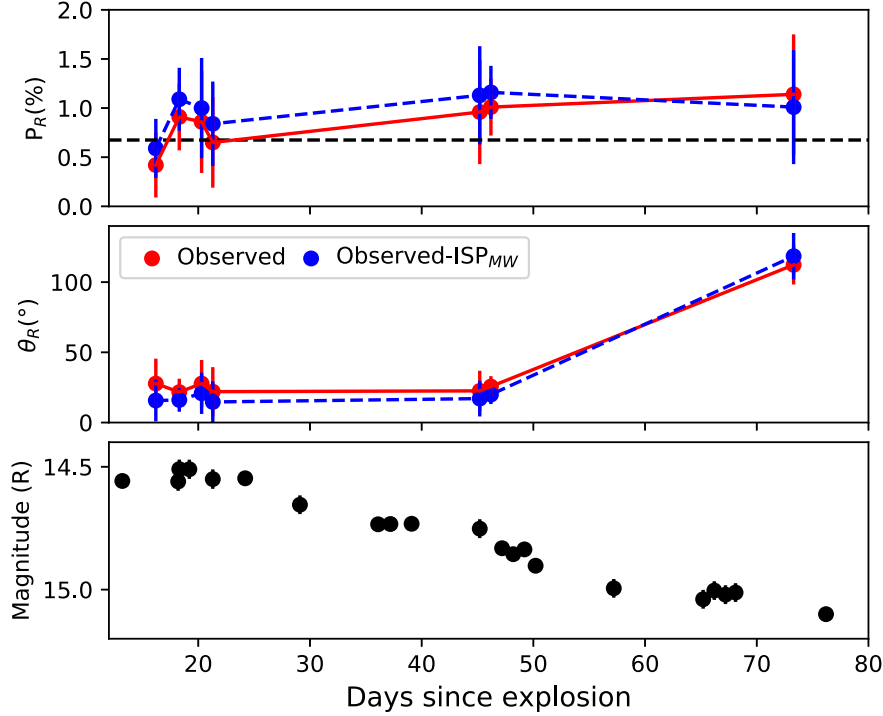


Figure 5. *Top panel:* Temporal evolution of degree of polarization in R -band (P_R) for SN 2016B. The horizontal dashed line represents the maximum amount of host galaxy polarization. *Middle panel:* Temporal evolution of polarization angle θ_R for SN 2016B. The observed polarization parameters are shown in dashed lines and the ISP_{MW} subtracted polarization parameters are shown in solid line. *Bottom panel:* R -band light curve of SN 2016B spanning the period of polarimetric observations.

Table 7. Polarimetric evolution of SN 2016B.

| UT date (yyyy-mm-dd) | JD 245 7000+ | Phase ^a (d) | Observed | | ISP_{MW} subtracted | |
|-------------------------|-----------------|---------------------------|------------------|--------------------|-----------------------|--------------------|
| | | | P_R (per cent) | θ_R (°) | P_R (per cent) | θ_R (°) |
| 2016-01-10.9 | 398.4 | 16.4 | 0.42 ± 0.33 | 27.77 ± 17.72 | 0.59 ± 0.30 | 15.69 ± 14.87 |
| 2016-01-13.0 | 400.5 | 18.5 | 0.91 ± 0.34 | 21.66 ± 9.56 | 1.09 ± 0.32 | 16.09 ± 8.39 |
| 2016-01-15.0 | 402.5 | 20.5 | 0.86 ± 0.52 | 27.77 ± 16.80 | 1.00 ± 0.51 | 20.84 ± 14.71 |
| 2016-01-16.0 | 403.5 | 21.5 | 0.65 ± 0.46 | 22.00 ± 17.47 | 0.84 ± 0.43 | 14.66 ± 14.67 |
| 2016-02-08.9 | 427.4 | 45.4 | 0.96 ± 0.53 | 22.56 ± 14.33 | 1.13 ± 0.50 | 17.06 ± 12.73 |
| 2016-02-09.9 | 428.4 | 46.4 | 1.01 ± 0.29 | 25.66 ± 7.39 | 1.16 ± 0.27 | 19.92 ± 6.76 |
| 2016-03-08.0 | 455.5 | 73.5 | 1.14 ± 0.61 | 112.32 ± 13.99 | 1.01 ± 0.58 | 118.48 ± 16.55 |

^aSince explosion epoch $t_0 = 2457\ 382.0$ JD (2015 December 25.4).

true bolometric luminosity is used in the analytical modelling as discussed in Section 7.3.

7.2 Mass of ^{56}Ni

The tail bolometric luminosity provides a tight constraint on the ^{56}Ni mass synthesized during the explosion since the early tail phase is powered by the decay of ^{56}Co , the daughter nucleus of ^{56}Ni , to ^{56}Fe . Below we use the tail bolometric luminosity to estimate the ^{56}Ni mass in two ways.

7.2.1 ^{56}Ni mass from SN 1987A

For SN 1987A, the mass of ^{56}Ni has been determined fairly accurately to be $0.075 \pm 0.005 M_\odot$ (Arnett 1996). Hence by assuming similar γ -ray energy deposition and comparing the bolometric luminosity with that of SN 1987A at a similar phase, we can estimate M_{Ni} of SN 2016B. For comparison, we use the $BVRI$ bolometric

luminosity at 188 d, which is $(9.52 \pm 0.28) \times 10^{40}$ and $(11.0 \pm 4.0) \times 10^{40}$ erg s^{-1} for SNe 1987A and SN 2016B, respectively. The ratio of luminosities of SN 2016B and SN 1987A is 1.16 ± 0.42 , and hence the value of M_{Ni} for SN 2016B is $0.087 \pm 0.032 M_\odot$.

7.2.2 ^{56}Ni mass from tail luminosity

The ^{56}Ni mass is estimated from the tail bolometric luminosity using the expression given in Hamuy (2003):

$$M_{Ni} = 7.866 \times 10^{-44} \times L_t \exp \left[\frac{(t - t_0)/(1 + z) - 6.1}{111.26} \right] M_\odot, \quad (10)$$

where t_0 is the explosion time, 6.1 d is the half-lifetime of ^{56}Ni , and 111.26 d is the e-folding time of the ^{56}Co decay. The tail luminosity (L_t) at ~ 152.5 and 188.1 d is $2.60 \pm 1.06 \times 10^{41}$ and $2.14 \pm 0.87 \times 10^{41}$ erg s^{-1} , respectively, which corresponds to a mean ^{56}Ni mass of $0.079 \pm 0.023 M_\odot$.

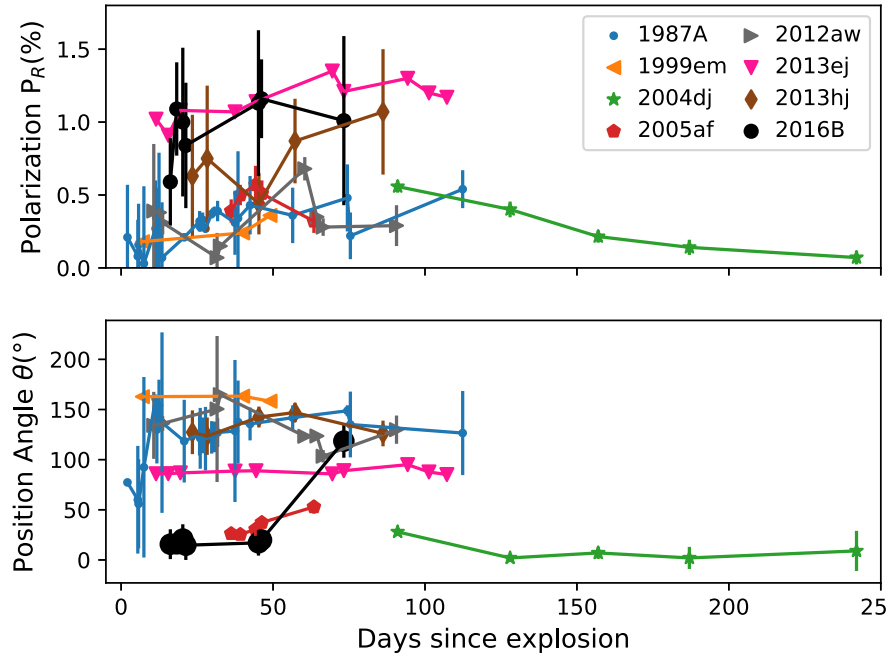


Figure 6. Temporal evolution of the ISP-subtracted polarization parameters of SN 2016B along with those of other Type II SNe.

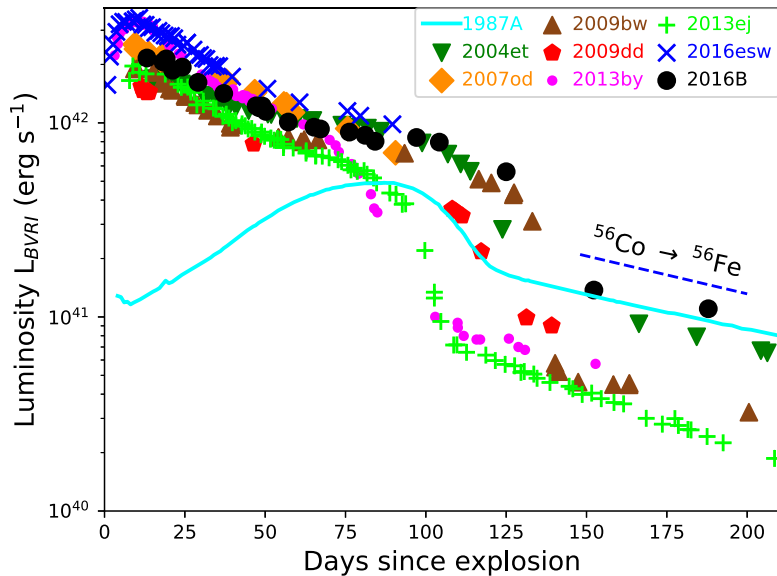


Figure 7. The *BVRl* pseudo-bolometric light curve of SN 2016B is compared with those of other SNe II from the comparison sample. The exponentially declining radioactive tail assuming full trapping of γ -ray photons and positrons is shown with dashed lines.

The above two methods yield consistent results and the weighted mean value of ^{56}Ni mass from these methods is $0.082 \pm 0.019 M_{\odot}$. SN 2016B, hence follows the mean absolute plateau magnitude at 50 d (M_V^{50}) and ^{56}Ni mass (M_{Ni}) correlation as shown in Fig. 8, which is reproduced using the data from Hamuy (2003), Spiro et al. (2014), and Valenti et al. (2015).

7.3 Semi-analytical modelling

The comparison of the true bolometric light curve with those generated from semi-analytic models can provide reliable estimates of the physical parameters of the explosion. The two-component

semi-analytic model with a dense inner core and an extended low-mass envelope developed by Nagy & Vinkó (2016) is used to generate the model light curves. The radiative diffusion model is used in this technique in order to incorporate the recombination energy to the total energy budget powering the light curve. This was originally developed by Arnett & Fu (1989) for a homologously expanding spherical ejecta, where the dominant source of opacity is assumed to be constant Thomson scattering opacity. The final bolometric luminosity is computed as the sum of the recombination energy and the energy liberated from radioactive decay of ^{56}Ni and ^{56}Co , taking the effect of gamma-ray leakage into consideration.

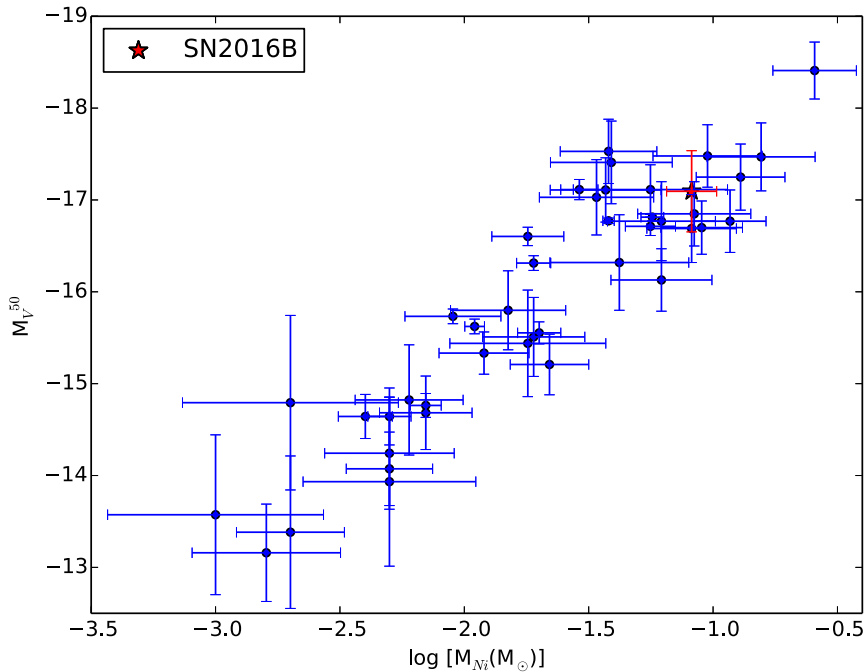


Figure 8. The position of SN 2016B in the absolute V-band magnitude at 50 d versus ^{56}Ni mass is shown. The data are taken from Hamuy (2003), Spiro et al. (2014), and Valenti et al. (2015).

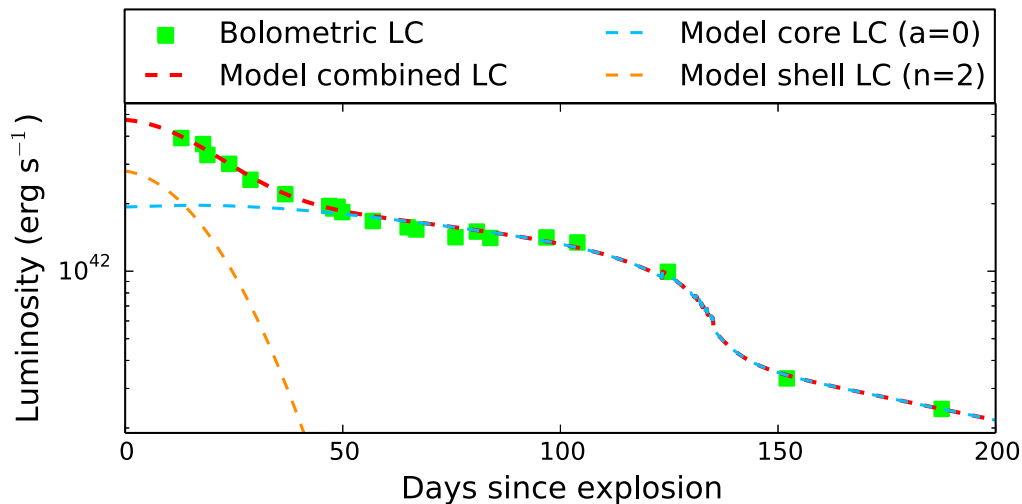


Figure 9. The best-fitting two-component analytical model of Nagy & Vinkó (2016) to the observed bolometric light curve of SN 2016B.

The expanding ejecta typically attains a constant density profile as it reaches the state of homologous expansion, while the outer part of the star develops a power-law density profile. We used a constant density profile for the core and a power-law density profile with index (n) 2 for the shell. Similar density profile for the shell has been used to model the light curve of SN 2013ej, another transitional object (see Nagy & Vinkó 2016 and Morozova et al. 2017, for a discussion). The best-fitting ejecta mass, progenitor radius and explosion energy are $14 M_{\odot}$, 2.8×10^{13} cm ($\sim 400 R_{\odot}$), and 1.4 foe respectively and the total ejecta mass, adding a shell mass of $0.53 M_{\odot}$ obtained from the modelling, is $14.5 M_{\odot}$. Assuming a core of $1.5 M_{\odot}$, the pre-SN star has a mass of $16 M_{\odot}$, which would mean

that the zero-age main-sequence (ZAMS) mass of the progenitor lies in the top edge of the Type II progenitor mass distribution (Smartt 2015). So far, the classical Type IIP SNe are found to arise from RSGs with ZAMS mass of $<15 M_{\odot}$, while Type IIL-like events have slightly more massive yellowish progenitors (Elias-Rosa et al. 2010; Fraser et al. 2010). Thus, the progenitor of SN 2016B appears to be in the borderline between Type IIP and IIL-like progenitors. However, one should be careful while quoting the ejecta mass (M_{ej}) estimate from semi-analytic light-curve models as the M_{ej} and opacity (κ) are strongly correlated parameters, and hence introduces significant uncertainty in the determination of these parameters. It is only their product ($M_{ej}\kappa$) which can be constrained from the modelling.

Table 8. The best-fitting core and shell parameters for true bolometric light curve of SN 2016B using Nagy & Vinkó (2016).

| Parameter | Core | Shell | Remarks |
|--|----------------------|---------------------|-------------------------------|
| R_0 (cm) | 2.8×10^{13} | 11×10^{13} | Initial radius of ejecta |
| T_{rec} (K) | 9500 | – | Recombination temperature |
| M_{ej} (M_{\odot}) | 14 | 0.53 | Ejecta mass |
| E_{th} (foe) | 0.7 | 0.037 | Initial thermal energy |
| E_{kin} (foe) | 0.7 | 0.073 | Initial kinetic energy |
| M_{Ni} (M_{\odot}) | 0.086 | – | Initial ^{56}Ni mass |
| κ ($\text{cm}^2 \text{g}^{-1}$) | 0.15 | 0.2 | Opacity |
| A_g (d^2) | 2.7×10^5 | 1×10^{10} | Gamma-ray leakage |

The mass of ^{56}Ni estimated from the fit is $0.086 M_{\odot}$, which is consistent with the value derived in Section 7.2 within errors.

The parameters of the outer shell can also be estimated using this model, like the radius of the H-envelope ($R = 11 \times 10^{13}$ cm). This can be considered as a lower limit, since dense sampling during the early phase is required for a reliable estimate. The true bolometric light curve with the best-fitting model is shown in Fig. 9. The parameters of the shell and core are listed in Table 8.

8 SPECTRAL ANALYSIS

The spectra of SN 2016B from 13.4 to 177.1 d from explosion are presented in chronological order in Fig. 10. H Balmer lines, the discerning feature of SNe II, are prominent throughout the evolution. Due to the multiple line blends, line identification in SN spectrum becomes difficult. We modelled the spectra of SN 2016B until the end of photospheric phase with SYN++ (Thomas, Nugent & Meza 2011) and a detailed line identification at two epochs, 13.4 and 65.3 d, which corresponds to the early and plateau phase of SN 2016B are shown in Fig. 11. SYN++ is an updated version of SYNOW (Fisher et al. 1997, 1999; Branch et al. 2002), which uses the Sobolev approximation to simplify the radiative transport problem, and produce synthetic spectra, once the free expansion phase of the SN ejecta has ceased. It assumes the formation of spectral lines by resonance scattering above a sharp photosphere and a homologously expanding ejecta.

8.1 Salient spectral features

The early spectra (13.4–19.4 d) are dominated by H I, He I, and Ca II H&K lines, which are fairly well-reproduced in the synthetic spectrum (Fig. 11). The proper fitting of the H δ model line in the observed spectra required the addition of Sr II ion in the modelling. An absorption dip bluewards of H α is seen and identified from the modelling as Si II $\lambda 6355$ (Fig. 10). The strength of this absorption feature is similar to H α at 13.4 d, becomes stronger than H α at 17.5 and 19.4 d, and then gradually weakens to disappear below the detection threshold at 57.3 d. From modelling, we tentatively identify a very weak feature bluewards of H β (marked as ‘A’ in Fig. 11), as C II $\lambda 4745$, which dies out after the 17.5 d spectrum. Two weak absorption dips at 4500 and 4583 Å marked with ‘?’ in Fig. 11 are identified as normal and high-velocity components of He II $\lambda 4686$.

The model fits to the H Balmer, Fe II, and Si II lines in the observed photospheric phase spectra (26.4–97.3 d) are shown in Fig. 12, in which we mark the high-velocity component of the H I lines conspicuous from the 57.3 d spectrum. In order to fit

the extended H α and H β profile, we used a combination of two velocity components i.e. variable normal velocity and constant high velocity (7000 km s^{-1}) components, to reproduce H I lines in the 57.3–97.3 d spectra. In Fig. 13, we generate model fits for the H I lines in the 65.3 d spectrum, with the low- and high-velocity (HV) component separately, to substantiate the point. The HV component may be arising from the excitation of the outer recombined ejecta by X-rays from the ejecta–CSM interaction in the photospheric phase (Chugai, Chevalier & Utrobin 2007). Further, during the late photospheric phase, a notch forms due to excitation of the cool dense shell behind the reverse shock, which is apparent in the H β feature in the spectra of SN 2016B. The stagnate nature of the HV component further strengthens the fact that this feature is not arising from the excitation of some metal line.

The early nebular phase spectra, at 152.5 and 177.1 d, are discerned by the appearance of forbidden lines of [O I] $\lambda 6300$, 6364 and [Ca II] $\lambda 7291$, 7324. Further, we tentatively classify the feature at around 8130 Å as a Ni I line blend. Other dominant elements in the nebular spectra are those with low quantum-level transitions, such as Na I and Ca II.

In Fig. 14, the evolution of the various prominent lines in the spectra of SN 2016B is shown. While the H α and H β lines form at higher velocity, and hence at larger radii at all phases, the Fe II, Sc II, and Ba II have nearly the same velocities and are formed at deeper layers of the ejecta.

8.2 Comparison to other SNe II

A comparison plot of the 13.4 d spectrum of SN 2016B along with other SNe II is shown in Fig. 15. While the Fe II lines are quite well-developed in SNe 1999em and 2004et at coeval epochs, these lines have not yet emerged in SN 2016B, indicating higher ejecta temperature in SN 2016B. The absorption dip bluewards of H α in the spectra of SN 2016B, identified as Si II $\lambda 6355$, is also conspicuous in the spectra of SNe 2004et, 2007od and 2013ej, although in SN 2004et this line is identified as the HV component of H α (Sahu et al. 2006).

The features in the plateau phase of SN 2016B is similar to those of other SNe II as shown in Fig. 16. HV component of H Balmer lines is prominent in SNe 2009bw, 2013ej, and 2016B giving rise to broad absorption feature. In SN 2013ej, this HV component evolves with time (Bose et al. 2015) and is non-evolving in SNe 2009bw (7300 km s^{-1} , Inserra et al. 2012) and 2016B (7000 km s^{-1}). SNe 2013ej and 2016B display the strongest O I $\lambda 7774$ feature at this phase, while SN 2009bw shows no evidence of oxygen.

Due to the decreasing velocity and low opacity of ejecta at the nebular phase, the P-Cygni absorption trough of H I and

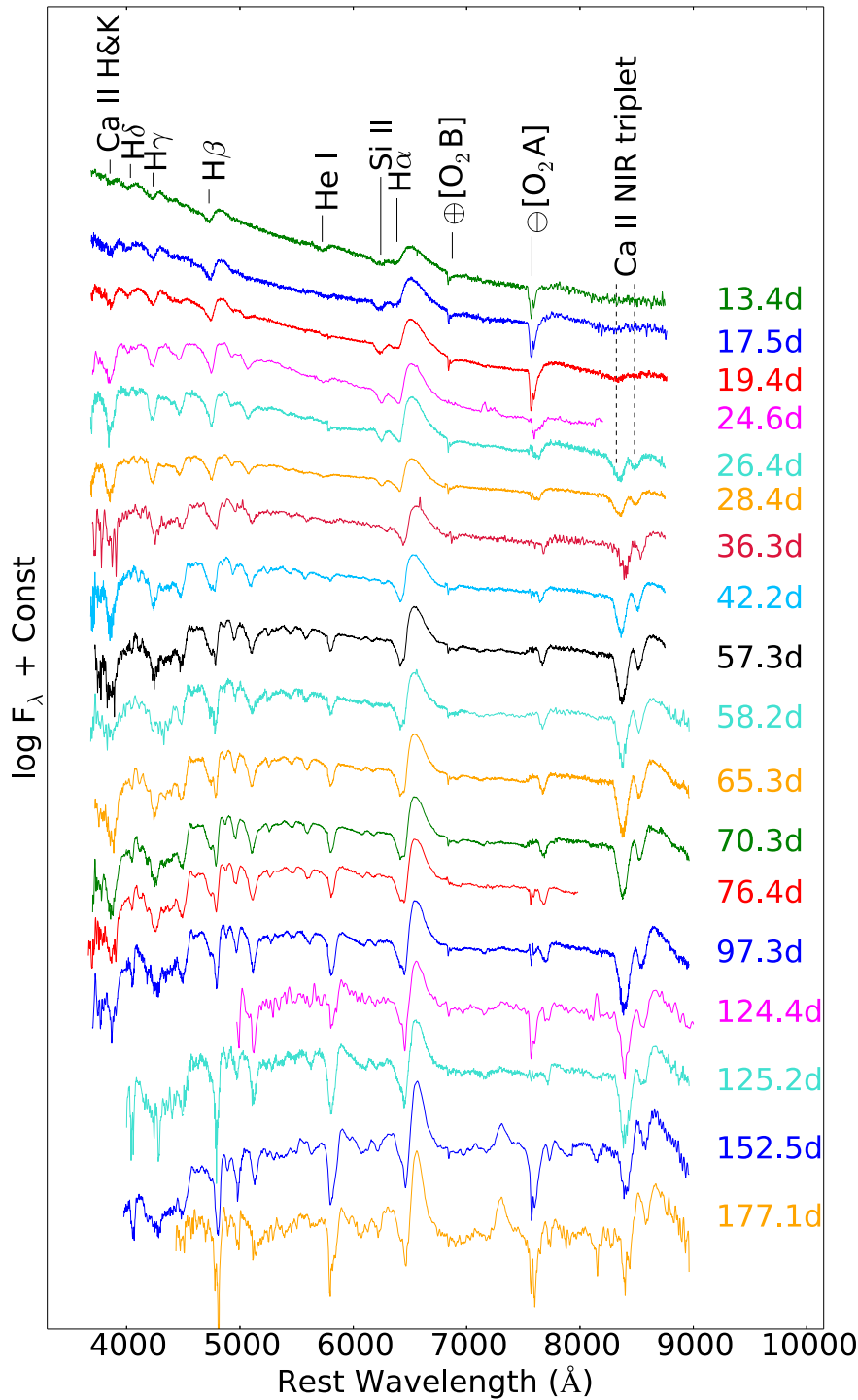


Figure 10. The spectral evolution of SN 2016B marked with the most prominent features in the spectra.

metal lines becomes narrower and weaker. The Ni line blend identified in the nebular spectra of SN 2016B at 8130 Å is also conspicuous in the spectra of SNe 1999em, 2004et, and 2009bw (Fig. 17).

8.3 Progenitor mass from nebular spectra

As suggested by Woosley & Weaver (1995), the nucleosynthetic yield depends strongly on the mass of progenitor, hence the observed

strengths of nebular lines can serve as a diagnostic of the progenitor mass. Jerkstrand et al. (2014) generated models of nebular spectra for 12, 15, 19, and 25 M_{\odot} progenitor for $0.062 M_{\odot}$ of ^{56}Ni , assuming a distance of 5.5 Mpc. In Fig. 18, we compare the 177 d spectrum of SN 2016B to these models to get a handle on the mass of progenitor. For the comparison, we scaled the model spectra with the ratio $(0.082/0.062)$ to correct for ^{56}Ni mass and then rescaled the 212 d model flux to the distance and phase (177 d) of the nebular spectrum of SN 2016B. The SN spectrum is de-redshifted,

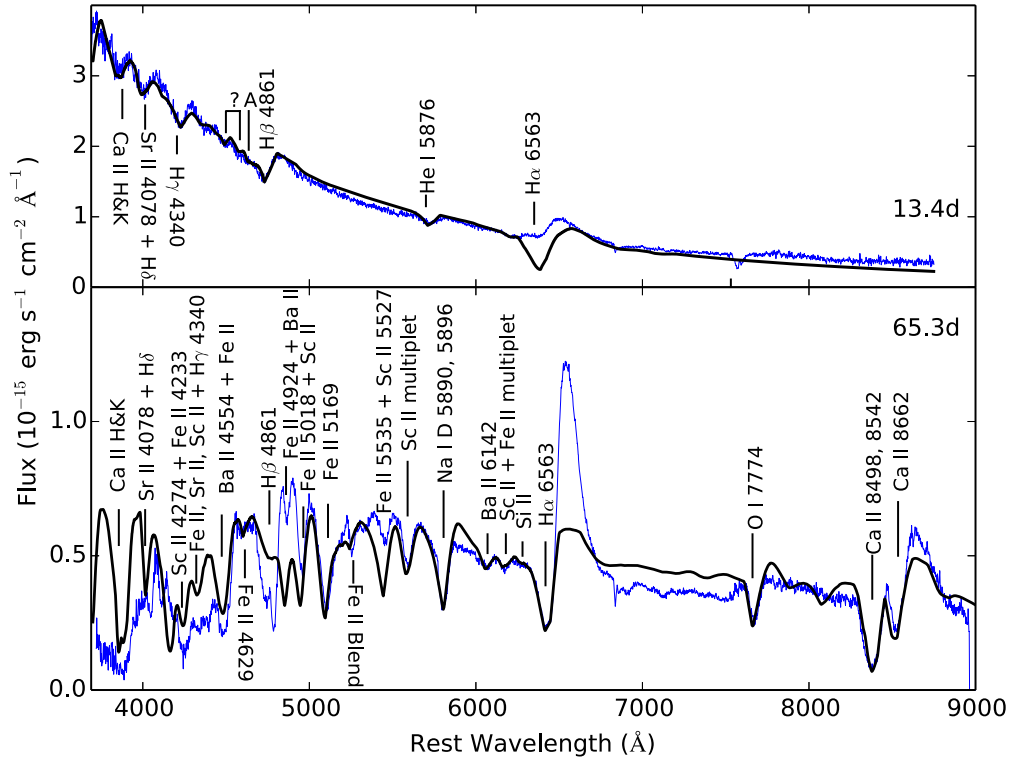


Figure 11. SYN++ modelling of the early (13.4 d) and plateau phase (65.3 d) spectra of SN 2016B marked with the lines identified from the modelling.

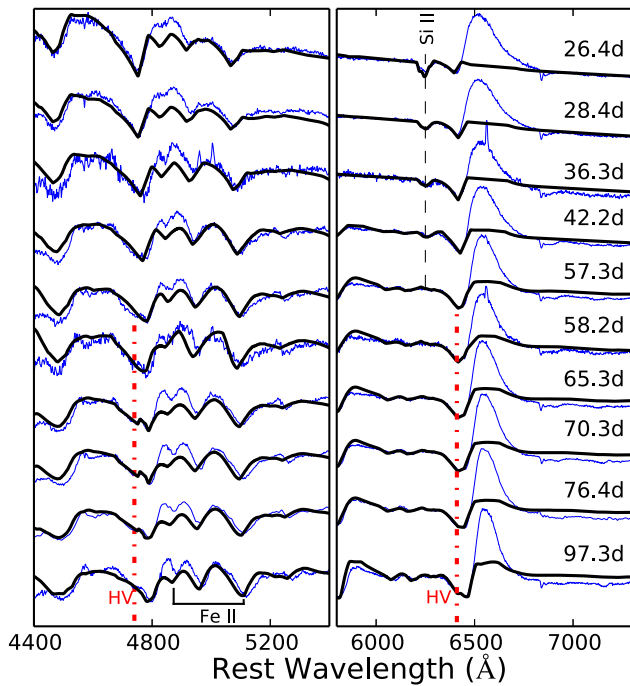


Figure 12. SYN++ modelling of the H Balmer, Fe II, and Si II lines in the spectra of SN 2016B shown at the photospheric phases. The broad, extended absorption feature of H I from the 57.3 d spectrum is reproduced using a normal velocity and a high-velocity component.

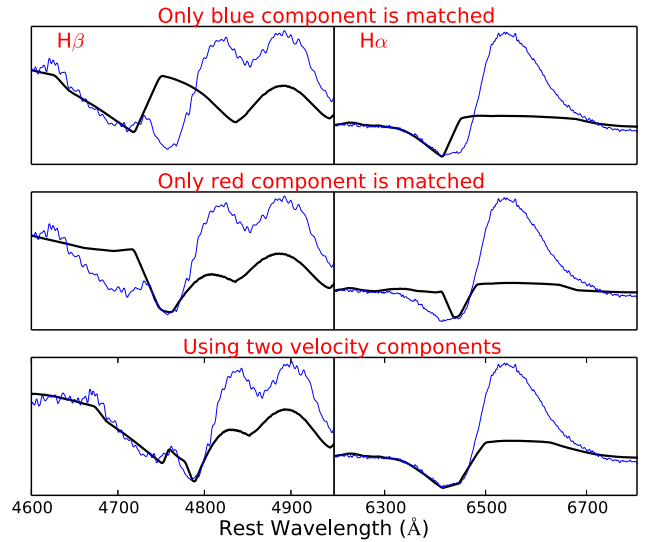


Figure 13. SYN++ fits for the H Balmer lines in the 65.3 d spectrum, with the HV component in the upper panel, normal velocity component in the middle panel and both components in the bottom panel.

dereddened, and corrected for flux losses using the photometric fluxes, before comparison.

We find that the model spectra reproduce strong H Balmer and Ca II NIR triplet features. The strong H I line could be arising from the uncertainty in mixing scheme used for bringing hydrogen clumps from the outer layers into the radioactive core. The

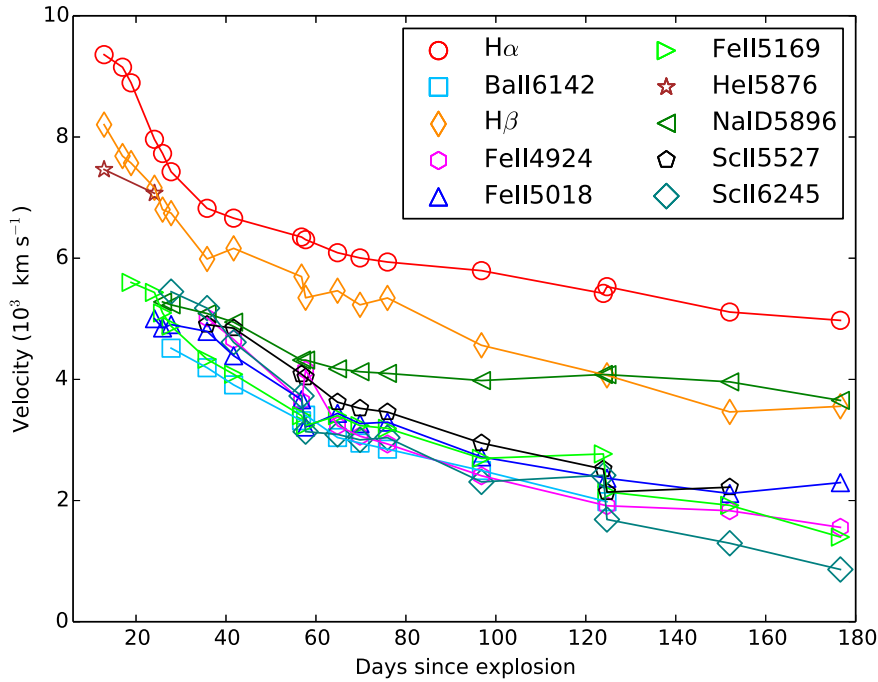


Figure 14. Velocity evolution of the prominent lines in the spectra of SN 2016B estimated from the shift in the P-Cygni absorption feature.

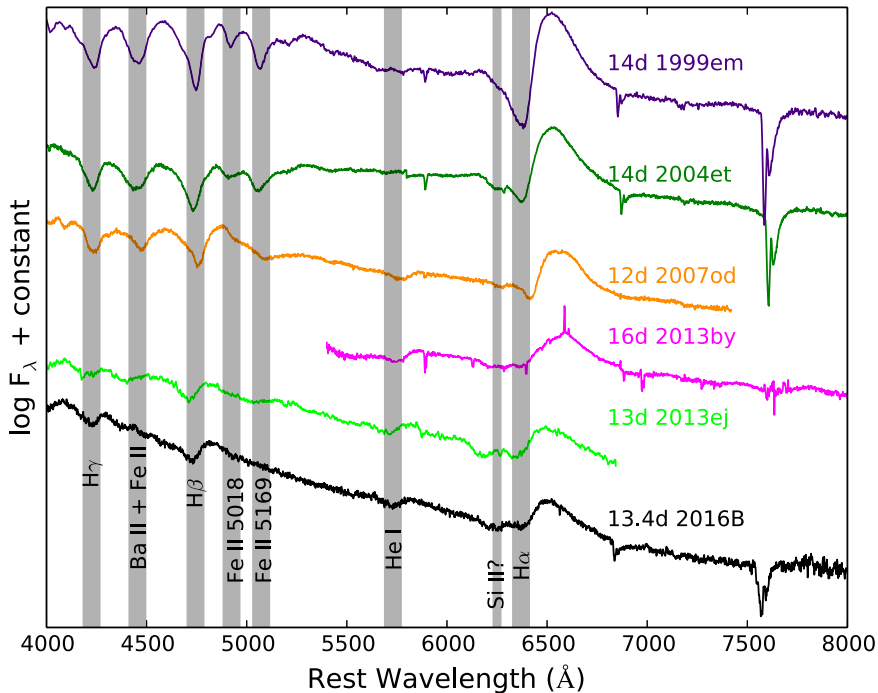


Figure 15. The early spectrum of SN 2016B at 13.4 d is compared with those of Type IIP and IIL SNe.

overestimated peak strength of Ca II NIR triplet is possibly due to a high-density envelope used in the model, scattering the Ca II $\lambda 8498$ and Ca II $\lambda 8542$ in Ca II $\lambda 8662$. The strength of [O I] $\lambda \lambda 6300, 6364$ in the 177 d spectrum of SN 2016B is more similar to that of the $15 M_{\odot}$ (ZAMS) model, while the 12 and $19 M_{\odot}$ models under- and overestimate the strength of the line, respectively. Also, the strength

of Na I D line in the spectrum of SN 2016B matches roughly with that of the $15 M_{\odot}$ model.

Oxygen is the most abundant element in the carbon ashes (the O/Ne/Mg layer) and hence a large fraction of the thermalized energy in this layer is reemitted by oxygen in the form of the nebular line [O I] $\lambda \lambda 6300, 6364$. Thus, the [O I] luminosity is a key to probe the

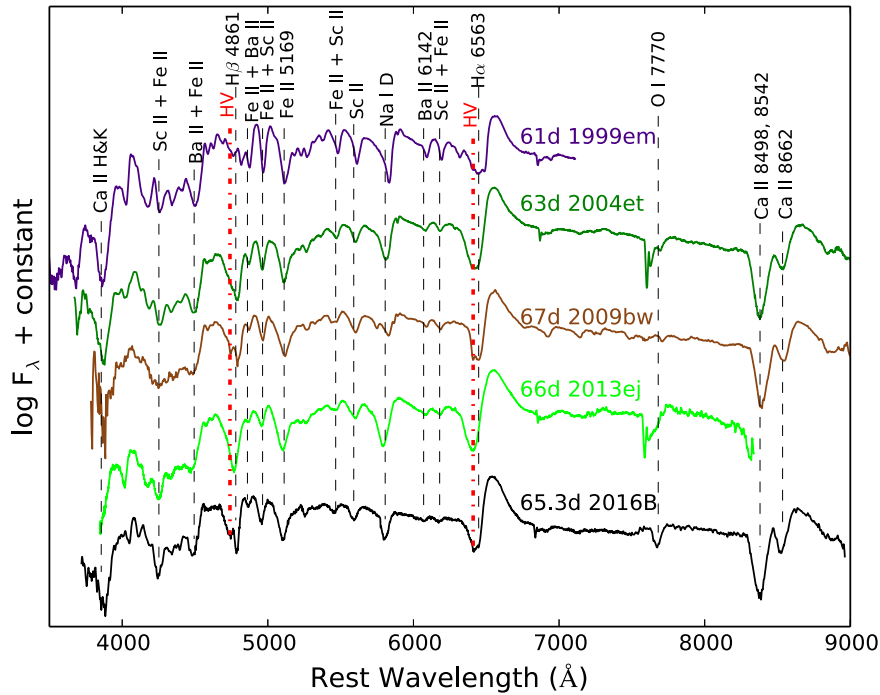


Figure 16. The plateau phase spectrum of SN 2016B at 65.3 d is compared with those of SNe II from the comparison sample.

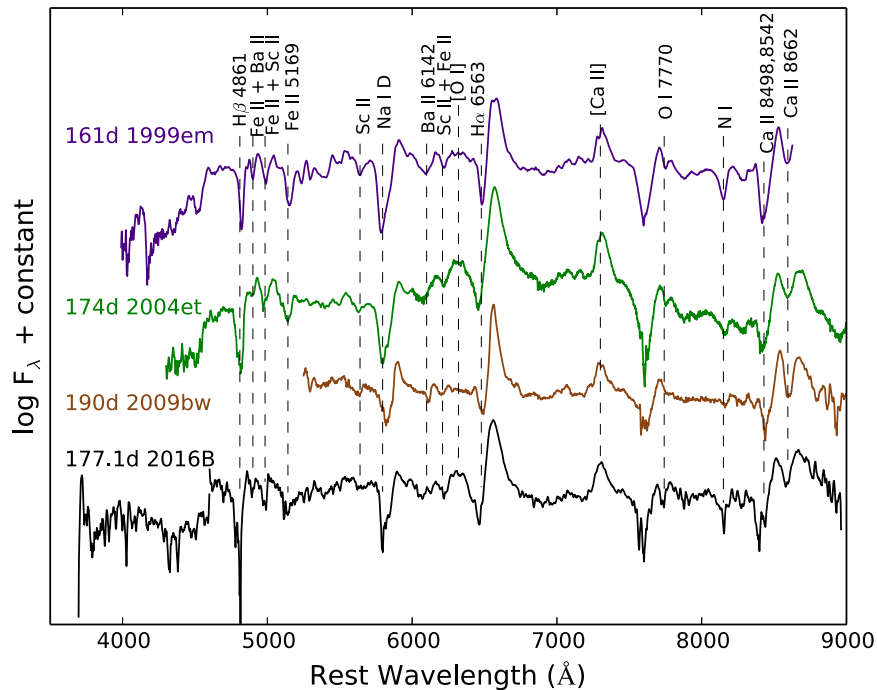


Figure 17. The comparison of the nebular phase spectrum of SN 2016B at 177.1 d with those of SNe II from the comparison sample.

amount of nucleosynthesized oxygen, which being highly sensitive to the helium core mass, is an indicator of the ZAMS mass (e.g. Woosley & Weaver 1995; Thielemann, Nomoto & Hashimoto 1996, however, see Ertl et al. 2016 for a different perspective). To better constrain the progenitor mass, we estimate the [O I] luminosity for SN 2016B in the 177 d spectrum and compare to that of the

model. The 212 d [O I] luminosity for the model spectra are 1.36 , 2.08 , and 3.19×10^{39} erg s^{-1} for 12, 15, and 19 M_{\odot} progenitor mass, respectively. After scaling the luminosities for ^{56}Ni mass and flux decline rate, the [O I] luminosities at 177 d are 2.00, 3.06, and 4.02×10^{39} erg s^{-1} for 12, 15, and 19 M_{\odot} model spectra, respectively. The [O I] luminosity for SN 2016B in the 177 d

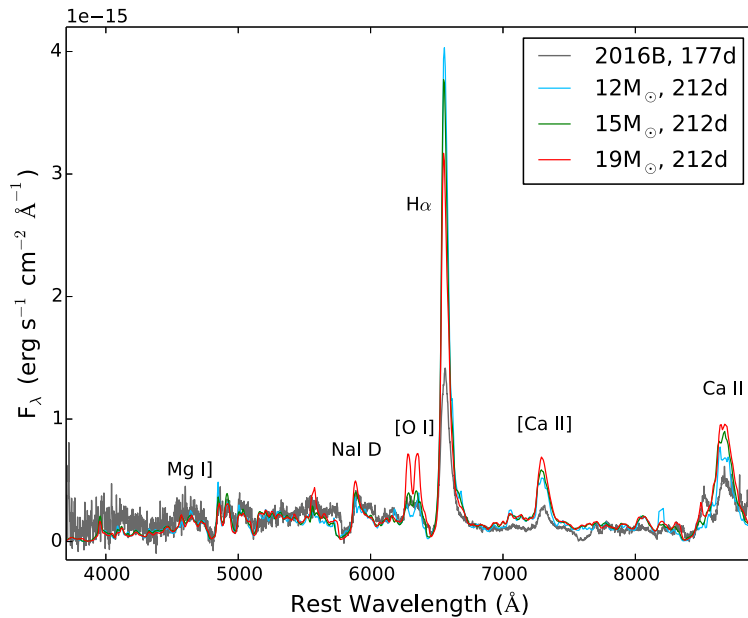


Figure 18. Comparison of the 177 d spectrum of SN 2016B with that of the scaled model spectra from Jerkstrand et al. (2014).

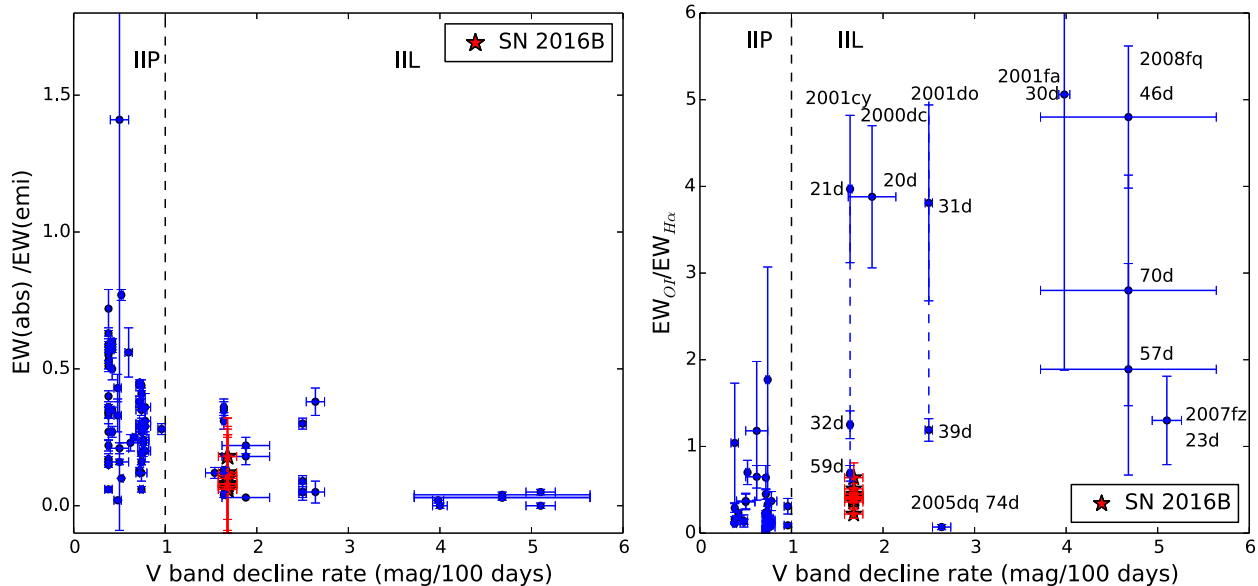


Figure 19. EW ratio of the absorption to emission feature of $H\alpha$ (left-hand panel) and EW ratio of $O\text{I } \lambda 7774$ and $H\alpha$ (right-hand panel) at different phases (26.4, 36.3, 42.2, 57.3, 58.2, 65.3, 70.3, 76.4, 97.3, and 125.2 d) in the spectra of SN 2016B (shown with red stars) compared with those in the Faran et al. (2014) sample of SN II. The dashed line demarcates the IIP/IIL regimes based on the early decline rate as suggested in Faran et al. (2014).

spectrum, obtained in a similar way as described in Jerkstrand et al. (2012), is $(2.66 \pm 0.97) \times 10^{39}$ erg s^{-1} , which indicates that the ZAMS mass of the progenitor lies in the range of 12–17 M_{\odot} , taking into account the error in luminosity. The derived ZAMS progenitor mass range includes the pre-supernova star mass estimated from analytical modelling of the light curve in Section 7.3.

9 SN 2016B: A TYPE IIP OR IIL SN?

SN 2016B displays photometric and spectroscopic properties intermediate to those of Type IIP and IIL SNe. The post-peak decline

rate in V band is steeper (0.84 mag 50 d $^{-1}$) than that suggested by Faran et al. (2014) to classify an SN as IIP and lasts up to ~ 66 d, while the plateau decline rate is shallow (0.24 mag 50 d $^{-1}$) extending up to ~ 118 d, and falls within the range of plateau slopes of SNe IIP. The steep drop from the plateau to the radioactive tail, a feature considered for long to be the signature of Type IIP SNe, is 1.6 ± 0.2 mag in 25 d in SN 2016B, in accord with the range of values in SNe II (1.0–2.6 mag; Valenti et al. 2016). However, this property has been noted in Type IIL SNe observed for a longer duration of time (Valenti et al. 2015). Further, the long optically thick phase duration of 118 d of SN 2016B, concurs with that of Type IIP SNe.

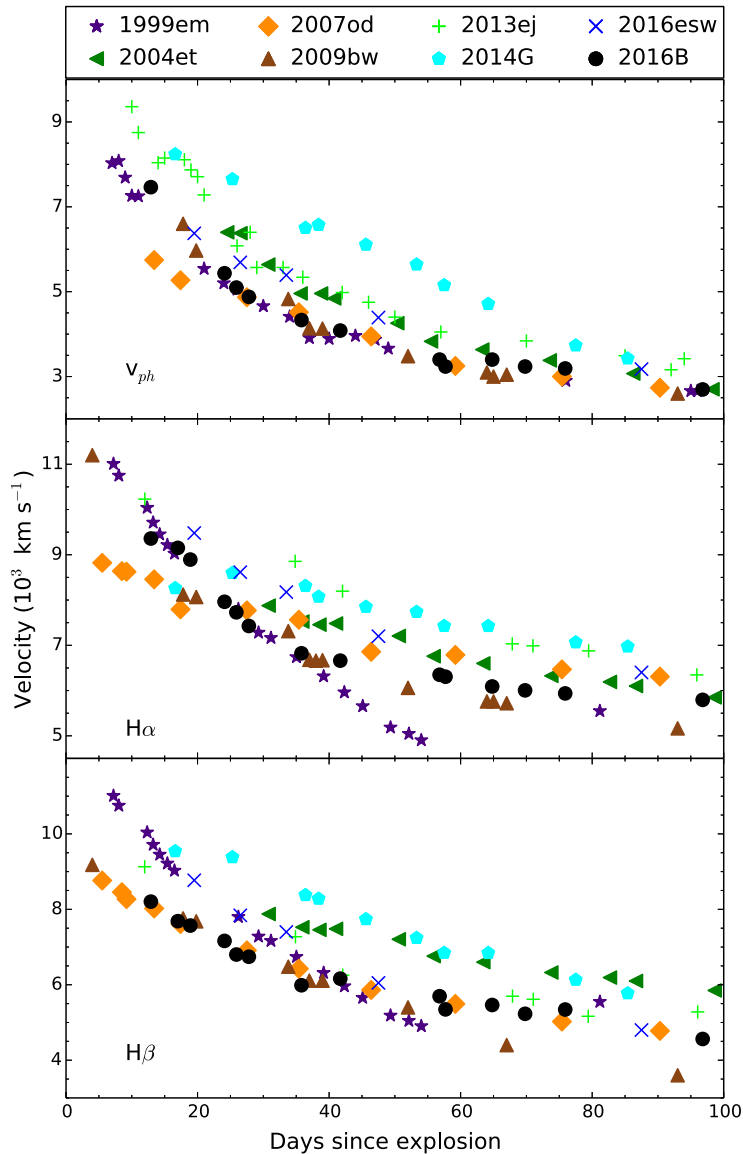


Figure 20. The comparison of photospheric (v_{ph} ; from the absorption minima of He I at early phases and Fe II 5169 at photospheric stage), H α and H β velocity evolution of SN 2016B with those of other Type II SNe.

While it is challenging to judge from spectroscopy whether an event is to be categorized as Type IIP or IIL, Patat et al. (1994) and Schlegel (1996) found from their analysis that SNe IIL have shallower H α P-Cygni profile than SNe IIP, which is reinforced in the studies of Gutiérrez et al. (2014) and Faran et al. (2014). This is possibly linked with the mass and density profile of hydrogen envelope in the pre-supernova star. Further, the metal lines (such as, O I $\lambda 7774$) in the spectra of SNe IIL are found to be stronger than that in SNe IIP, which results from the rapid recombination wave in SNe IIL, leading to a highly dense photosphere. Thus, in order to discern the collocation of SN 2016B in the SN II zoo from its spectral properties, we reproduce the absorption to emission ratio of H α (a/e) versus V -band decline rate and $EW_{O I}/EW_{H\alpha}$ versus V -band decline rate plots from Faran et al. (2014) in Fig. 19. In the former, we find that SN 2016B belongs to Type IIL class, and in the latter, the O I line is weaker than in most Type IIL SNe, and is more similar to Type IIP SNe. Besides, the HV feature discernable

in the H I lines at the photospheric phase, endorses SN 2016B as a Type IIL SN.

Moreover, Faran et al. (2014) suggested a higher photospheric velocity and shallower H I velocity evolution profiles of SNe IIL with respect to SNe IIP. The flatter velocity profile of H I in SNe IIL is attributed to the formation of absorption troughs in the outer, higher velocity layers above the photosphere, as the photosphere recedes into the hydrogen poor layers during the photospheric stage. We compare the photospheric velocity of SN 2016B (computed from the blue-shifted absorption trough of Fe II and Sc II lines at photospheric phase and He I line at early phase) with those of other SNe II in the top panel of Fig. 20. The photospheric velocity of SN 2016B is similar to SNe 1999em, 2007od, and 2009bw, whereas, the velocity is lower by about 500–600 km s $^{-1}$ than SNe 2013ej, 2004et, and 2016esw. The middle and bottom panel of Fig. 20 shows the velocity evolution of H α and H β lines, respectively. In both the plots, SNe 1999em and 2009bw exhibit a power-law decline,

typical of Type IIP, while the flatter evolution of H I line velocity is apparent in SNe 2004et (Sahu et al. 2006), 2007od (Inserra et al. 2011), 2013ej (Bose et al. 2015), 2014G (Terreran et al. 2016), 2016esw (de Jaeger et al. 2018), and 2016B, typical of Type IIL.

The progenitors of SNe II detected in pre-explosion *HST* images and reported in Smartt (2015) are found to have masses below $15 M_{\odot}$ for most SNe IIP and are slightly more massive, yellow supergiants for SNe IIL. Further, we estimate the progenitor mass of SN 2016B by comparing the nebular spectrum to late-time spectral models. These methods yield values corresponding to the upper end of the range of masses of progenitors detected for SNe II ($16.5 \pm 1.5 M_{\odot}$), which commonly give rise to SNe IIL. From the above discussion, we conclude that SN 2016B exhibits intermediate properties in the SN II diversity.

10 CONCLUSIONS

In this paper, we present the analysis of the photometric, polarimetric, and spectroscopic observations of SN 2016B in the galaxy PGC 037392. The post-peak decline in SN 2016B is steeper than most SNe classified as Type IIP in the literature. However, the optically thick phase duration is longer than SNe IIL lasting up to 118 d. In addition, the maximum recorded luminosity in *V* band in the present study and the plateau decline rate does not corroborate with the correlation deduced from a sample of SNe II by Anderson et al. (2014). The plateau decline rate of SN 2016B quoted in a recent paper by Gutiérrez et al. (2018) as $0.34 \pm 0.01 \text{ mag } 100 \text{ d}^{-1}$, which is within errors of our derived value ($0.47 \pm 0.24 \text{ mag } 100 \text{ d}^{-1}$). The low cadence photometric follow-up during the recombination phase is possibly the cause of the high error in our quoted light curve parameters, however, we could determine all the parameters reasonably well.

We also report *R*-band polarimetric observations of SN 2016B. SN 2016B displays significant, but nearly constant intrinsic polarization throughout our observation period spanning from the early cooling to the recombination phase. Though the polarization angle shows an abrupt change at 73.5 d, we do not step into a conclusion as we do not have observation of any nearby epoch to support this value. The polarization of SN 2016B, considering the maximum host galaxy polarization coaligned with the SN polarization, is about 0.3–0.4 per cent, which is typical of hydrogen-rich Type II SNe in the photospheric phase.

We derived the ^{56}Ni mass from the tail luminosity to be $0.082 \pm 0.019 M_{\odot}$. Thus, SN 2016B falls within the plateau luminosity versus ^{56}Ni mass correlation for SNe II (Hamuy 2003; Spiro et al. 2014; Valenti et al. 2015). The explosion parameters derived from analytical modelling of the true bolometric light curve indicates a total ejecta mass of $\sim 15 M_{\odot}$, an initial radius of $400 R_{\odot}$ and a total explosion energy of 1.4 foe. The progenitor mass derived by comparing the nebular spectrum of SN 2016B to the spectral models from Jerkstrand et al. (2014), suggests a 12–17 M_{\odot} ZAMS progenitor.

Broad absorption troughs of H I lines are apparent from the 57.3 d spectrum, which we reproduced with a combination of normal velocity and constant HV component in SYN++ modelling. HV component of H I lines indicates a possible role of circumstellar interaction, more evident in Type IIL SNe. Moreover, the spectra of SN 2016B exhibit weaker absorption profile of H I lines similar to Type IIL SNe whereas weaker metal lines such as O I 7774 line unlike Type IIL SNe. The transitional nature of SN 2016B showing resemblance to both the photometric and spectroscopic properties of Type IIP and IIL, blurs out the fine line demarcating these two

types, suggesting a continuum of properties in the hydrogen-rich SNe II family.

ACKNOWLEDGEMENTS

This work is partially based on observations collected at Copernico 1.82m telescope (Asiago, Italy) of the INAF – Osservatorio Astronomico di Padova. We thank N. Elias-Rosa for the NOT observations. This work made use of The Neil Gehrels *Swift*/UVOT data reduced by P. J. Brown and released in the *Swift* Optical/Ultraviolet Supernova Archive (SOUSA). SOUSA is supported by NASA’s Astrophysics Data Analysis Program through grant NNX13AF35G. This research has made use of the NASA/IPAC Extragalactic Database (NED) which is operated by the Jet Propulsion Laboratory, California Institute of Technology, under contract with the National Aeronautics and Space Administration. We acknowledge the usage of the HyperLeda data base (<http://leda.univ-lyon1.fr>). This work has made use of data from the European Space Agency (ESA) mission *Gaia* (<https://www.cosmos.esa.int/gaia>), processed by the *Gaia* Data Processing and Analysis Consortium DPAC, <https://www.cosmos.esa.int/web/gaia/dpac/consortium>). Funding for the DPAC has been provided by national institutions, in particular the institutions participating in the *Gaia* Multilateral Agreement. SBP and KM acknowledges BRICS grant DST/IMRCD/BRICS/Pilotcall/ProFCheap/2017(G) for this work. KM acknowledges the support from the IUSSTF WISTEMM fellowship and UC Davis. AP, LT, and SB are partially supported by the PRIN-INAF 2016 with the project ‘Towards the SKA and CTA era: discovery, localization, and physics of transient sources’ (P.I. M. Giroletti). BK acknowledges the Science and Engineering Research Board (SERB) under the Department of Science & Technology, Govt. of India, for financial assistance in the form of National Post-doctoral Fellowship (Ref. no. PDF/2016/001563).

REFERENCES

- Anderson J. P. et al., 2014, *ApJ*, 786, 67
 Arcavi I. et al., 2012, *ApJ*, 756, L30
 Arnett D., 1996, *Supernovae and Nucleosynthesis: An Investigation of the History of Matter from the Big Bang to the Present*, Princeton University Press, Princeton, NJ
 Arnett W. D., Fu A., 1989, *ApJ*, 340, 396
 Barbon R., Ciatti F., Rosino L., 1979, *A&A*, 72, 287
 Barrett P., 1988, *MNRAS*, 234, 937
 Beers T. C., Kriessler J. R., Bird C. M., Huchra J. P., 1995, *AJ*, 109, 874
 Bersten M. C., Hamuy M., 2009, *ApJ*, 701, 200
 Bessell M. S., Castelli F., Plez B., 1998, *A&A*, 333, 231
 Blondin S., Tonry J. L., 2007, *ApJ*, 666, 1024
 Bose S. et al., 2015, *ApJ*, 806, 160
 Bose S., Kumar B., Misra K., Matsumoto K., Kumar B., Singh M., Fukushima D., Kawabata M., 2016, *MNRAS*, 455, 2712
 Branch D. et al., 2002, *ApJ*, 566, 1005
 Breeveld A. A., Landsman W., Holland S. T., Roming P., Kuin N. P. M., Page M. J., 2011, in McEnery J. E., Racusin J. L., Gehrels N., eds, *AIP Conf. Proc. Vol. 1358, Gamma Ray Burst 2010*. Am. Inst. Phys., New York, p. 373
 Brown P. J. et al., 2009, *AJ*, 137, 4517
 Brown P. J., Breeveld A. A., Holland S., Kuin P., Pritchard T., 2014, *Ap&SS*, 354, 89
 Chevalier R. A., 1986, *ApJ*, 308, 225
 Chornock R., Filippenko A. V., Li W., Silverman J. M., 2010, *ApJ*, 713, 1363
 Chugai N. N., 2006, *Astron. Lett.*, 32, 739

- Chugai N. N., Fabrika S. N., Sholukhova O. N., Goranskij V. P., Abolmasov P. K., Vlasjuk V. V., 2005, *Astron. Lett.*, 31, 329
- Chugai N. N., Chevalier R. A., Utrobin V. P., 2007, *ApJ*, 662, 1136
- Dastidar R. et al., 2018, *MNRAS*, 479, 2421
- de Jaeger T. et al., 2018, *MNRAS*, 478, 3776
- Dessart L., Hillier D. J., 2011, *MNRAS*, 415, 3497
- Dhungana G. et al., 2016, *ApJ*, 822, 6
- Elias-Rosa N. et al., 2010, *ApJ*, 714, L254
- Ertl T., Janka H.-T., Woosley S. E., Sukhbold T., Ugliano M., 2016, *ApJ*, 818, 124
- Eswaraiah C., Maheswar G., Pandey A. K., Jose J., Ramaprakash A. N., Bhatt H. C., 2013, *A&A*, 556, A65
- Faran T. et al., 2014, *MNRAS*, 445, 554
- Fisher A., Branch D., Nugent P., Baron E., 1997, *ApJ*, 481, L89
- Fisher A., Branch D., Hatano K., Baron E., 1999, *MNRAS*, 304, 67
- Fraser M. et al., 2010, *ApJ*, 714, L280
- Gaia Collaboration, 2016, *A&A*, 595, A1
- Gaia Collaboration, 2018, *A&A*, 616, A1
- Gehrels N. et al., 2004, *ApJ*, 611, 1005
- Gutiérrez C. P. et al., 2014, *ApJ*, 786, L15
- Gutiérrez C. P. et al., 2017, *ApJ*, 850, 89
- Gutiérrez C. P. et al., 2018, *MNRAS*, 479, 3232
- Hamuy M., 2003, *ApJ*, 582, 905
- Hamuy M., Pinto P. A., 2002, *ApJ*, 566, L63
- Hamuy M., Suntzeff N. B., 1990, *AJ*, 99, 1146
- Hamuy M. et al., 2001, *ApJ*, 558, 615
- Höflich P., Wheeler J. C., Hines D. C., Trammell S. R., 1996, *ApJ*, 459, 307
- Höflich P., Wheeler J. C., Wang L., 1999, *ApJ*, 521, 179
- Hough J. H., Bailey J. A., Rouse M. F., Whittet D. C. B., 1987, *MNRAS*, 227, 1P
- Huang F. et al., 2015, *ApJ*, 807, 59
- Inserra C. et al., 2011, *MNRAS*, 417, 261
- Inserra C. et al., 2012, *MNRAS*, 422, 1122
- Inserra C. et al., 2013, *A&A*, 555, A142
- Jeffery D. J., 1991, *ApJ*, 375, 264
- Jerkstrand A., Fransson C., Maguire K., Smartt S., Ergon M., Spyromilio J., 2012, *A&A*, 546, A28
- Jerkstrand A., Smartt S. J., Fraser M., Fransson C., Sollerman J., Taddia F., Kotak R., 2014, *MNRAS*, 439, 3694
- Jordi K., Grebel E. K., Ammon K., 2006, *A&A*, 460, 339
- Karachentsev I. D., Nasonova O. G., Karachentseva V. E., 2015, *Astrophys. Bull.*, 70, 1
- Kumar B., Pandey S. B., Eswaraiah C., Gorosabel J., 2014, *MNRAS*, 442, 2
- Kumar B., Pandey S. B., Eswaraiah C., Kawabata K. S., 2016, *MNRAS*, 456, 3157
- Landolt A. U., 2009, *AJ*, 137, 4186
- Leonard D. C. et al., 2002a, *PASP*, 114, 35
- Leonard D. C. et al., 2006, *Nature*, 440, 505
- Leonard D. C. et al., 2016, *IAU Focus Meeting*, 29, 458
- Leonard D. C., Filippenko A. V., 2001, *PASP*, 113, 920
- Leonard D. C., Filippenko A. V., Ardila D. R., Brotherton M. S., 2001, *ApJ*, 553, 861
- Leonard D. C., Filippenko A. V., Chornock R., Foley R. J., 2002b, *PASP*, 114, 1333
- Leonard D. C., Kanbur S. M., Ngeow C. C., Tanvir N. R., 2003, *ApJ*, 594, 247
- Li W. et al., 2011, *MNRAS*, 412, 1441
- Lusk J. A., Baron E., 2017, *PASP*, 129, 044202
- Maguire K. et al., 2010, *MNRAS*, 404, 981
- Mauerhan J. C. et al., 2017, *ApJ*, 834, 118
- Medhi B. J., Maheswar G., Pandey J. C., Kumar T. S., Sagar R., 2008, *MNRAS*, 388, 105
- Melson T., Janka H.-T., Marek A., 2015, *ApJ*, 801, L24
- Misra K., Pooley D., Chandra P., Bhattacharya D., Ray A. K., Sagar R., Lewin W. H. G., 2007, *MNRAS*, 381, 280
- Morozova V., Piro A. L., Valenti S., 2017, *ApJ*, 838, 28
- Müller B., 2016, *Publ. Astron. Soc. Aust.*, 33, e048
- Nagy A. P., Vinkó J., 2016, *A&A*, 589, A53
- Olivares E. F. et al., 2010, *ApJ*, 715, 833
- Pandey J. C., Medhi B. J., Sagar R., Pandey A. K., 2009, *MNRAS*, 396, 1004
- Patat F., Barbon R., Cappellaro E., Turatto M., 1994, *A&A*, 282, 731
- Pereyra A., Magalhães A. M., Rodrigues C. V., Silva C. R., Campos R., Hickel G., Cieslinski D., 2006, *A&A*, 454, 827
- Phillips M. M. et al., 2013, *ApJ*, 779, 38
- Piascik A. S., Steele I. A., 2016, *Astron. Telegram*, 8505, 1
- Ramaprakash A. N., Gupta R., Sen A. K., Tandon S. N., 1998, *A&AS*, 128, 369
- Rautela B. S., Joshi G. C., Pandey J. C., 2004, *Bull. Astron. Soc. India*, 32, 159
- Riess A. G. et al., 2016, *ApJ*, 826, 56
- Roberts L. F., Ott C. D., Haas R., O'Connor E. P., Diener P., Schnetter E., 2016, *ApJ*, 831, 98
- Roming P. W. A. et al., 2005, *Space Sci. Rev.*, 120, 95
- Sahu D. K., Anupama G. C., Srividya S., Muneer S., 2006, *MNRAS*, 372, 1315
- Sanders N. E. et al., 2015, *ApJ*, 799, 208
- Schlafly E. F., Finkbeiner D. P., 2011, *ApJ*, 737, 103
- Schlegel E. M., 1996, *AJ*, 111, 1660
- Schmidt G. D., Elston R., Lupie O. L., 1992, *AJ*, 104, 1563
- Serkowski K., Mathewson D. S., Ford V. L., 1975, *ApJ*, 196, 261
- Shappee B. J. et al., 2016, *Astron. Telegram*, 8502, 1
- Smartt S. J., 2015, *Publ. Astron. Soc. Aust.*, 32, e016
- Spiro S. et al., 2014, *MNRAS*, 439, 2873
- Srivastav S., Ninan J. P., Kumar B., Anupama G. C., Sahu D. K., Ojha D. K., Prabhu T. P., 2016, *MNRAS*, 457, 1000
- Stetson P. B., 1987, *PASP*, 99, 191
- Stetson P. B., 1992, *J. R. Astron. Soc. Can.*, 86, 71
- Terreran G. et al., 2016, *MNRAS*, 462, 137
- Thielemann F.-K., Nomoto K., Hashimoto M.-A., 1996, *ApJ*, 460, 408
- Thomas R. C., Nugent P. E., Meza J. C., 2011, *PASP*, 123, 237
- Valenti S. et al., 2015, *MNRAS*, 448, 2608
- Valenti S. et al., 2016, *MNRAS*, 459, 3939
- van Dokkum P. G., 2001, *PASP*, 113, 1420
- Wang L., Wheeler J. C., 2008, *ARA&A*, 46, 433
- Wang L., Wheeler J. C., Li Z., Clocchiatti A., 1996, *ApJ*, 467, 435
- Wang L. et al., 2003a, *ApJ*, 591, 1110
- Wang L., Baade D., Höflich P., Wheeler J. C., 2003b, *ApJ*, 592, 457
- Woosley S. E., Weaver T. A., 1995, *ApJS*, 101, 181
- Young T. R., 2004, *ApJ*, 617, 1233
- Yuan F. et al., 2016, *MNRAS*, 461, 2003

APPENDIX A: PHOTOMETRY

The UV photometry was obtained from *Swift* Optical/Ultraviolet Supernova Archive (SOUSA; <https://archive.stsci.edu/prepds/sou sa/>; Brown et al. 2014). The reduction is based on that of Brown et al. (2009), including subtraction of the host galaxy count rates and uses the revised UV zero-points and time-dependent sensitivity from Breeveld et al. (2011). The *Swift* UVOT magnitudes are given in Table A2.

We performed point spread function (PSF) fitting photometry on the optical data using DAOPHOT II (Stetson 1987), pre-processing the images with bias subtraction, flat-fielding and cosmic ray removal (L.A. COSMIC, van Dokkum 2001). Since SN 2016B exploded in the outskirts of the host galaxy, a careful selection of the aperture for PSF photometry is sufficient to eliminate any host galaxy contribution to the SN flux. The first aperture used for photometry is the mean FWHM of the frame, while the sky flux is estimated in an 8 pixel wide annular region with an inner radius which is four times the FWHM.

Further, to convert the instrumental magnitudes to the standard magnitudes, a set of local standard stars were generated in the SN

Table A1. Summary of the instruments used for the observational campaign of SN 2016B.

| Telescope | Location | Instrument | Pixel scale | Imaging | Dispersers/grisms | |
|--|---|-----------------|-------------------------------|---------|-------------------|---|
| | | | (arcsec pixel ⁻¹) | bands | | |
| 1.04m Sampurnanand Telescope (ST) | ARIES Observatory, India | Tek 1k×1k | 0.53 | VRI | – | 1 |
| 1.3m Devasthal Fast Optical Telescope (DFOT) | ARIES Observatory, India | Andor 512 × 512 | 0.64 | UBVRI | – | 2 |
| 1.82m Copernico Telescope | Asiago, Mount Ekar (Italy) | AFOSC | 0.48 | uBVgriz | Gr04, VPH6 | 3 |
| 2.01m Himalayan Chandra Telescope (HCT) | Indian Astronomical Observatory, Hanle, India | HFOSC | 0.296 | UBVRI | Gr7, Gr8 | 4 |
| 2.56m Nordic Optical Telescope (NOT) | Roque de los Muchachos, La Palma, Canaris (Spain) | ALFOSC | 0.19 | uBVgriz | – | 5 |
| 3.58m Telescopio Nazionale Galileo (TNG) | Roque de los Muchachos, La Palma, Canaris (Spain) | DOLORES | 0.252 | BVgriz | LR-B, LR-R | 6 |
| 3.6m Devasthal Optical Telescope (DOT) | ARIES Observatory, India | 4k×4k | 0.19 (2 × 2 bin) | R | – | 7 |

Table A2. *Swift* UVOT photometry.

| UT date (yyyy-mm-dd) | JD 2457 000+ | Phase ^a (d) | uvw2 (mag) | uvm2 (mag) | uvw1 (mag) | uvu (mag) | uvb (mag) | uvv (mag) |
|-------------------------|-----------------|---------------------------|---------------|---------------|---------------|--------------|--------------|--------------|
| 2016-01-03.5 | 391.1 | 9.1 | 13.97 ± 0.05 | 13.87 ± 0.06 | 13.49 ± 0.04 | 13.57 ± 0.04 | 14.82 ± 0.05 | 14.81 ± 0.06 |
| 2016-01-06.3 | 393.8 | 11.8 | 14.53 ± 0.06 | 14.15 ± 0.05 | 13.87 ± 0.05 | 13.70 ± 0.04 | 14.81 ± 0.05 | 14.88 ± 0.06 |
| 2016-01-07.8 | 395.3 | 13.3 | 14.71 ± 0.06 | 14.56 ± 0.06 | 14.06 ± 0.05 | 13.76 ± 0.04 | 14.82 ± 0.05 | 14.77 ± 0.06 |
| 2016-01-10.1 | 397.6 | 15.6 | 15.31 ± 0.07 | 15.10 ± 0.06 | 14.60 ± 0.06 | 13.96 ± 0.04 | 14.85 ± 0.05 | 14.84 ± 0.06 |
| 2016-01-11.8 | 399.3 | 17.3 | 15.72 ± 0.08 | 15.53 ± 0.06 | 14.97 ± 0.06 | 14.09 ± 0.05 | 14.89 ± 0.05 | 14.92 ± 0.06 |
| 2016-01-14.2 | 401.7 | 19.7 | 16.36 ± 0.09 | 16.15 ± 0.07 | 15.52 ± 0.07 | 14.42 ± 0.05 | 14.95 ± 0.05 | 14.94 ± 0.06 |
| 2016-01-16.1 | 403.9 | 21.9 | 16.98 ± 0.11 | 16.76 ± 0.08 | 16.10 ± 0.08 | 14.75 ± 0.05 | 15.09 ± 0.05 | 14.97 ± 0.06 |
| 2016-01-17.6 | 405.1 | 23.1 | 17.29 ± 0.13 | – | 16.28 ± 0.09 | 14.93 ± 0.06 | 15.18 ± 0.05 | – |

^aSince explosion epoch $t_0 = 2457\,382.0$ JD (2015 December 25.4).

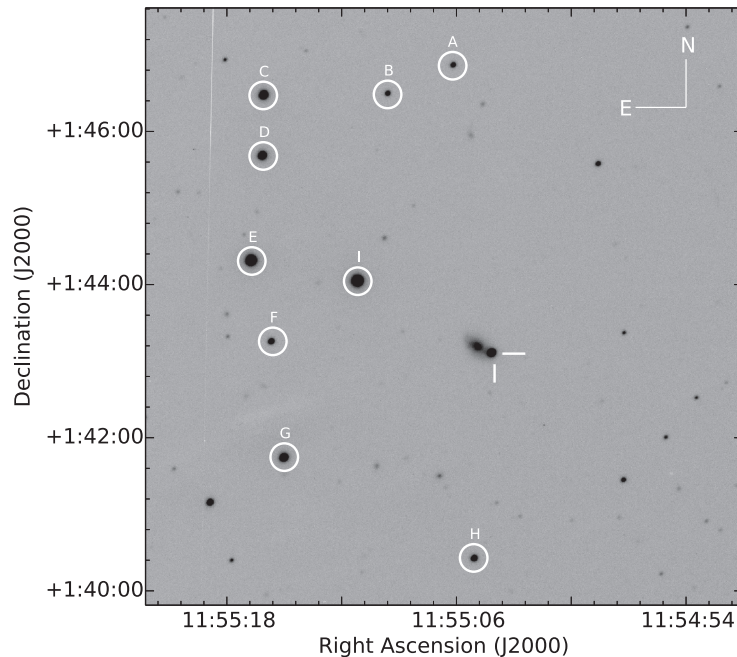
**Figure A1.** Local standards in the field of PGC 037392 marked along with SN 2016B. The V-band image was acquired on 2016 January 07 with the 2.01 m HCT.

Table A3. Coordinates and photometry of the local sequence reference stars in the *UBVRI* bands.

| ID | $\alpha_{J2000.0}$ (hh:mm:ss) | $\delta_{J2000.0}$ (dd:mm:ss) | <i>U</i> (mag) | <i>B</i> (mag) | <i>V</i> (mag) | <i>R</i> (mag) | <i>I</i> (mag) |
|----|----------------------------------|----------------------------------|-------------------|-------------------|-------------------|-------------------|-------------------|
| A | 11:55:06.2 | +01:46:51.5 | 17.380 (0.045) | 17.371 (0.009) | 16.760 (0.009) | 16.375 (0.010) | 16.037 (0.009) |
| B | 11:55:09.6 | +01:46:29.0 | 19.181 (0.096) | 17.974 (0.012) | 16.849 (0.009) | 16.235 (0.010) | 15.695 (0.006) |
| C | 11:55:16.1 | +01:46:28.2 | 15.212 (0.038) | 14.826 (0.007) | 14.202 (0.008) | 13.837 (0.010) | 13.524 (0.007) |
| D | 11:55:16.1 | +01:45:40.8 | 14.984 (0.038) | 14.892 (0.007) | 14.410 (0.007) | 14.085 (0.010) | 13.808 (0.006) |
| E | 11:55:16.7 | +01:44:18.5 | 14.451 (0.039) | 14.027 (0.007) | 13.380 (0.007) | 13.024 (0.009) | 12.725 (0.006) |
| F | 11:55:15.6 | +01:43:15.5 | 17.026 (0.042) | 16.612 (0.025) | 16.055 (0.008) | 15.676 (0.009) | 15.362 (0.008) |
| G | 11:55:15.0 | +01:41:44.8 | 15.507 (0.040) | 15.156 (0.051) | 14.621 (0.007) | 14.268 (0.009) | 13.961 (0.007) |
| H | 11:55:05.1 | +01:40:25.8 | 17.330 (0.047) | 16.717 (0.007) | 15.822 (0.008) | 15.341 (0.009) | 14.900 (0.005) |

Table A4. Optical photometry of SN 2016B.

| UT date (yyyy-mm-dd) | JD 2457 000+ | Phase ^a (d) | <i>U</i> (mag) | <i>B</i> (mag) | <i>V</i> (mag) | <i>R</i> (mag) | <i>I</i> (mag) | <i>Tel</i> |
|-------------------------|-----------------|---------------------------|-------------------|-------------------|-------------------|-------------------|-------------------|------------|
| 2016-01-07.9 | 395.4 | 13.4 | – | 14.65 ± 0.02 | 14.73 ± 0.03 | 14.56 ± 0.03 | 14.48 ± 0.01 | HCT |
| 2016-01-12.9 | 400.4 | 18.4 | 14.40 ± 0.07 | 14.76 ± 0.02 | 14.78 ± 0.03 | 14.56 ± 0.04 | 14.47 ± 0.01 | HCT |
| 2016-01-12.9 | 400.5 | 18.5 | 14.44 ± 0.07 | 14.76 ± 0.02 | 14.70 ± 0.03 | 14.51 ± 0.04 | 14.51 ± 0.01 | DFOT |
| 2016-01-13.9 | 401.4 | 19.4 | 14.54 ± 0.07 | 14.77 ± 0.02 | 14.66 ± 0.03 | 14.51 ± 0.04 | 14.50 ± 0.01 | DFOT |
| 2016-01-15.9 | 403.5 | 21.5 | 14.76 ± 0.05 | 15.13 ± 0.02 | 14.74 ± 0.03 | 14.55 ± 0.04 | 14.52 ± 0.01 | DFOT |
| 2016-01-18.9 | 406.4 | 24.4 | – | – | 14.74 ± 0.03 | 14.55 ± 0.03 | 14.51 ± 0.01 | DFOT |
| 2016-01-19.2 | 406.6 | 24.6 | 14.86 ± 0.04 | 14.97 ± 0.02 | 14.77 ± 0.03 | 14.59 ± 0.02 | 14.54 ± 0.02 | EKAR |
| 2016-01-23.8 | 411.3 | 29.3 | 15.50 ± 0.07 | 15.38 ± 0.02 | 14.94 ± 0.03 | 14.65 ± 0.04 | 14.52 ± 0.01 | HCT |
| 2016-01-30.8 | 418.3 | 36.3 | – | – | – | 14.73 ± 0.03 | 14.59 ± 0.01 | ST |
| 2016-01-31.8 | 419.3 | 37.3 | – | 15.77 ± 0.02 | – | – | – | DFOT |
| 2016-01-31.9 | 419.4 | 37.4 | – | – | 15.00 ± 0.03 | 14.73 ± 0.03 | 14.59 ± 0.01 | ST |
| 2016-02-02.8 | 421.3 | 39.3 | – | – | – | 14.73 ± 0.02 | 14.64 ± 0.01 | ST |
| 2016-02-08.9 | 427.4 | 45.4 | – | – | – | 14.75 ± 0.04 | 14.68 ± 0.01 | DFOT |
| 2016-02-10.8 | 429.4 | 47.4 | 16.89 ± 0.04 | 16.02 ± 0.02 | 15.20 ± 0.03 | – | – | DFOT |
| 2016-02-10.8 | 429.4 | 47.4 | – | – | – | 14.83 ± 0.03 | 14.66 ± 0.01 | ST |
| 2016-02-11.8 | 430.4 | 48.4 | 16.88 ± 0.05 | 16.04 ± 0.02 | 15.23 ± 0.03 | 14.86 ± 0.02 | 14.70 ± 0.01 | DFOT |
| 2016-02-12.9 | 431.4 | 49.4 | 16.83 ± 0.06 | 15.98 ± 0.02 | 15.21 ± 0.03 | 14.84 ± 0.03 | 14.69 ± 0.01 | DFOT |
| 2016-02-13.9 | 432.4 | 50.4 | 17.04 ± 0.04 | 16.10 ± 0.02 | 15.28 ± 0.03 | 14.90 ± 0.03 | 14.73 ± 0.01 | DFOT |
| 2016-02-14.9 | 433.5 | 51.5 | – | – | 15.44 ± 0.03 | – | 14.71 ± 0.04 | ST |
| 2016-02-20.9 | 439.4 | 57.4 | 17.14 ± 0.07 | 16.38 ± 0.02 | 15.43 ± 0.03 | 14.99 ± 0.04 | 14.76 ± 0.01 | HCT |
| 2016-02-28.8 | 447.4 | 65.4 | – | 16.52 ± 0.02 | 15.50 ± 0.03 | 15.04 ± 0.04 | 14.82 ± 0.01 | HCT |
| 2016-02-29.8 | 448.4 | 66.4 | – | – | 15.58 ± 0.04 | 15.00 ± 0.04 | 14.81 ± 0.01 | ST |
| 2016-03-01.8 | 449.4 | 67.4 | – | – | – | 15.02 ± 0.04 | 14.82 ± 0.01 | ST |
| 2016-03-02.0 | 449.5 | 67.5 | – | 16.68 ± 0.02 | 15.52 ± 0.03 | – | – | NOT |
| 2016-03-02.8 | 450.3 | 68.3 | – | – | 15.65 ± 0.03 | 15.01 ± 0.04 | 14.82 ± 0.01 | ST |
| 2016-03-07.8 | 455.3 | 73.3 | – | 16.59 ± 0.02 | – | – | – | DFOT |
| 2016-03-10.9 | 458.4 | 76.4 | 17.84 ± 0.09 | 16.69 ± 0.03 | 15.49 ± 0.04 | 15.10 ± 0.01 | – | EKAR |
| 2016-03-15.8 | 463.3 | 81.3 | – | – | 15.73 ± 0.04 | 15.01 ± 0.04 | 14.83 ± 0.01 | ST |
| 2016-03-18.9 | 466.4 | 84.4 | – | – | 15.82 ± 0.04 | 15.09 ± 0.04 | 14.90 ± 0.01 | ST |
| 2016-03-31.8 | 479.3 | 97.3 | 17.88 ± 0.07 | 16.81 ± 0.02 | 15.65 ± 0.03 | 15.12 ± 0.04 | 14.90 ± 0.01 | HCT |
| 2016-04-07.9 | 486.4 | 104.4 | – | – | 15.72 ± 0.03 | 15.19 ± 0.03 | 14.96 ± 0.01 | HCT |
| 2016-04-28.7 | 507.2 | 125.2 | – | 17.54 ± 0.02 | 16.12 ± 0.03 | 15.51 ± 0.04 | 15.23 ± 0.01 | HCT |
| 2016-05-02.7 | 511.2 | 129.2 | – | – | 16.33 ± 0.04 | 15.64 ± 0.03 | 15.42 ± 0.01 | ST |
| 2016-05-25.9 | 534.5 | 152.5 | – | 19.31 ± 0.03 | 18.10 ± 0.05 | – | – | TNG |
| 2016-05-26.7 | 535.2 | 153.2 | – | – | – | 16.87 ± 0.03 | 16.45 ± 0.02 | ST |
| 2016-06-30.6 | 570.1 | 188.1 | – | – | 18.10 ± 0.04 | 17.26 ± 0.04 | 16.74 ± 0.02 | HCT |
| 2017-04-02.9 | 847.0 | 465.0 | – | – | – | 19.79 ± 0.05 | – | DOT |

^aSince explosion epoch $t_0 = 2457\,382.0$ JD (2015 December 25.4).

field. To this end, observations of three Landolt standard fields (Landolt 2009), namely, PG 0918, PG 1047, and PG 1323, were carried out on 2016 February 28 under photometric night conditions (median FWHM seeing in *V* band ~ 2 arcsec) with the 2.01m Himalayan Chandra Telescope (HCT) at Indian Astronomical Observatory (IAO), Hanle. These fields were observed at three altitudes

covering airmass from 1.176 to 1.773. The *V*-band magnitudes of the stars in the standard field lie in the range 12.08–14.49 mag and the *B* – *V* colour varies between –0.290 and 1.044 mag. With the aid of the instrumental and standard magnitudes of the Landolt field stars, the zero-points, colour coefficients, and extinction values of the transformation equations were fitted using the least-square

linear regression technique as described in Stetson (1992) and the values thus obtained are given below:

$$\begin{aligned}
 u &= U + (3.40 \pm 0.27) + (0.08 \pm 0.13)(B - V) \\
 &\quad + (0.36 \pm 0.16)X \\
 b &= B + (1.28 \pm 0.02) + (-0.004 \pm 0.020)(B - V) \\
 &\quad + (0.20 \pm 0.02)X \\
 v &= V + (0.71 \pm 0.03) + (-0.08 \pm 0.04)(B - V) \\
 &\quad + (0.12 \pm 0.03)X \\
 r &= R + (0.79 \pm 0.05) + (-0.16 \pm 0.08)(V - R) \\
 &\quad + (0.08 \pm 0.05)X \\
 i &= I + (1.026 \pm 0.005) + (-0.027 \pm 0.004)(V - I) \\
 &\quad + (0.055 \pm 0.005)X,
 \end{aligned}$$

where X is the airmass. The rms scatter between the observed and standard magnitudes of the Landolt field stars are 0.08 mag in U , 0.03 mag in V , and 0.02 mag in BRI bands. We used these coefficients to generate a photometric sequence of eight non-

variable stars in the SN field. The eight local standards are marked in Fig. A1 and their magnitudes are tabulated in Table A3. The final SN magnitudes (listed in Table A4) are then obtained differentially with respect to the local standards by estimating the nightly zero-points. The errors in the magnitudes are the combined PSF fitting and photometric calibration errors propagated in quadrature.

APPENDIX B: SPECTROSCOPY

We removed the detector signatures from the frames using standard tasks in IRAF. The one-dimensional spectra extracted using the *APALL* task, were wavelength and flux calibrated using arc lamps and spectrophotometric standard star spectra, respectively, obtained at a similar airmass on the same night or a close-by night. To validate the wavelength calibration, night sky emission lines were used, and shifts were applied when necessary. A scaling factor to match the spectroscopic and photometric continuum flux is multiplied to the calibrated spectra to account for slit losses. Finally each spectrum was de-redshifted to the host galaxy rest frame using the *DOPCOR* task.

Table B1. Log of the spectroscopic observations.

| Date | Phase ^a (d) | Grism | Spectral range (Å) | Resolution | Instrument | Telescope |
|------------|---------------------------|------------|-----------------------|------------|------------|-----------|
| 2016-01-07 | 13.4 | Gr7, Gr8 | 3800–6840, 5800–9000 | 1330, 2190 | HFOSC | HCT |
| 2016-01-11 | 17.5 | Gr7, Gr8 | 3800–6840, 5800–9000 | 1330, 2190 | HFOSC | HCT |
| 2016-01-13 | 19.4 | Gr7, Gr8 | 3800–6840, 5800–9000 | 1330, 2190 | HFOSC | HCT |
| 2016-01-19 | 24.6 | Gr04 | 3360–7740 | 311 | AFOSC | EKAR |
| 2016-01-20 | 26.4 | Gr7, Gr8 | 3800–6840, 5800–9000 | 1330, 2190 | HFOSC | HCT |
| 2016-01-22 | 28.4 | Gr7, Gr8 | 3800–6840, 5800–9000 | 1330, 2190 | HFOSC | HCT |
| 2016-01-30 | 36.3 | Gr7, Gr8 | 3800–6840, 5800–9000 | 1330, 2190 | HFOSC | HCT |
| 2016-02-05 | 42.2 | Gr7, Gr8 | 3800–6840, 5800–9000 | 1330, 2190 | HFOSC | HCT |
| 2016-02-20 | 57.3 | Gr7, Gr8 | 3800–6840, 5800–9000 | 1330, 2190 | HFOSC | HCT |
| 2016-02-21 | 58.2 | Gr7, Gr8 | 3800–6840, 5800–9000 | 1330, 2190 | HFOSC | HCT |
| 2016-02-28 | 65.3 | Gr7, Gr8 | 3800–6840, 5800–9000 | 1330, 2190 | HFOSC | HCT |
| 2016-03-04 | 70.3 | Gr7, Gr8 | 3800–6840, 5800–9000 | 1330, 2190 | HFOSC | HCT |
| 2016-03-10 | 76.4 | Gr04 | 3360–7740 | 311 | AFOSC | EKAR |
| 2016-03-31 | 97.3 | Gr7, Gr8 | 3800–6840, 5800–9000 | 1330, 2190 | HFOSC | HCT |
| 2016-04-27 | 124.4 | VPH6 | 4500–10000 | 500 | AFOSC | EKAR |
| 2016-04-28 | 125.2 | Gr7, Gr8 | 3800–6840, 5800–9000 | 1330, 2190 | HFOSC | HCT |
| 2016-05-25 | 152.5 | LR-B, LR-R | 3000–8430, 4470–10073 | 585, 714 | DOLORES | TNG |
| 2016-06-19 | 177.1 | Gr7, Gr8 | 3800–6840, 5800–9000 | 1330, 2190 | HFOSC | HCT |

^aSince explosion epoch $t_0 = 2457382.0$ JD (2015 December 25.4).

This paper has been typeset from a $\text{\TeX}/\text{\LaTeX}$ file prepared by the author.